Petroleum Science 20 (2023) 3736–3751

Contents lists available at ScienceDirect

Petroleum Science

journal homepage: www.keaipublishing.com/en/journals/petroleum-science

Original Paper

Pressure evolution in shock-compacted granular media

Jia-Rui Li [a], Jun-Sheng Zeng [b], Kun Xue [a, *]

[a] State Key Laboratory of Explosive Science and Technology, Beijing Institute of Technology, Beijing, 100081, China
[b] Institute of Applied Physics and Computational Mathematics, Beijing, 100094, China

ARTICLE INFO

Article history:
Received 11 January 2023
Received in revised form
18 April 2023
Accepted 18 April 2023
Available online 19 April 2023

Edited by Jia-Jia Fei

Keywords:
Shock compaction
Pressure evolution
Transport in porous media
Transient gas infiltration
Mobile granular column

ABSTRACT

The pressure evolution associated with the transient shock-induced infiltration of gas flow through granular media consisting of mobile particles is numerically investigated using a coupled Eulerian −Lagrangian approach. The coupling between shock compaction and interstitial flow has been revealed. A distinctive two-stage diffusing pressure field with deflection occurring at the tail of the compaction front is found, with corresponding spikes in both gaseous velocity and temperature profiles emerging within the width of the compaction front. The compaction front, together with the deflection pressure, reaches a steady state during the later period. An analytical prediction of the steady deflection pressure that considers the contributions of porosity and the non-isothermal effect is proposed. The isothermal single-phase method we developed, combining the porosity jump condition across the compaction front, shows consistent pressure evolution with the non-isothermal CMP-PIC one under weak shock strength and low column permeability. Lastly, the microscale mechanism governing the formation of not only pressure deflection but also gaseous velocity and temperature spikes within the width of the compaction front has been described. These aforementioned evolutions of the flow field are shown to arise from the nozzling effects associated with the particle-scale variations in the volume fraction.

1. Introduction

The shock-induced damage and transformation process finds many applications in geotechnical engineering, including dynamic compaction, shock densification, laser cutting and drilling of rocks, hydraulic fracturing, rejuvenation of depleted borewell, etc. (Goodarzi et al., 2015; Jagadeesh, 2008; Thallak, 1991; Xie et al., 2021; Xu et al., 2020). Specifically, shock wave fracking has become an alternative to hydraulic fracturing in shale rocks. Reservoir deposits like Shale are formed of smectite minerals. Due to the swelling property of smectite, the water used in hydraulic fracturing reacts with the minerals and becomes trapped in the reservoir, impeding the flow of gas into the well. Therefore, shock wave fracking has a clear advantage in such situations, preventing the clay mineral from swelling. Another important application is related to increasing the yield of a depleted borewell using shock waves. The high pressure behind the shock travelling into the borewell acts normal to the walls of the borewell and helps in clearing the clogged-up water channels (fissures, fractures, etc.) present in rock formations, where water easily flows into the well.

The fundamental process underpinning these engineering applications is the dynamic responses of shale rock, which can be simplified as the assembly of densely packed cemented mineral grains subject to the impingement of shock waves. Understanding the build-up of the interstitial pressure in the shock compacting grains is critical to predicting resultant pneumatic fractures and to improving design and diagnosis for engineering applications. Considerable experimental and numerical efforts have been dedicated to investigating the shock interaction with granular media consisting of mobile or immobile particles (Poroshyna and Utkin, 2021; Zhang et al., 2022). Shock tube experiments provide insights into the evolution of the diffusion pressure as gases infiltrate through the interparticle pores as well as the propagation and attenuation of stress waves sustained in the solid skeleton (Britan et al., 2001). The stochastic nature of granular media results in large variability between experimental results, making it difficult to compare results from different granular media and draw generalized scaling laws. In contrast, in numerical investigations, this variability is either eliminated by considering the granular media as

* Corresponding author.
E-mail address: xuekun@bit.edu.cn (K. Xue).

https://doi.org/10.1016/j.petsci.2023.04.017

homogeneous continuum materials or properly smoothing out the variability by averaging over a number of assemblies with a stochastic arrangement of particles.

Numerical approaches wherein granular media are approximated as homogeneous continuum materials can be roughly classified into single-phase and two-phase approaches (Jafari et al., 2020; Skews, 2001; Sundaresan et al., 2018). In the single-phase approach, the solid skeleton is assumed to be motionless, and the particle-gas interactions are described by the flow resistance, including viscous and inertial resistances, known as the Darcy term and Forchheimer term, respectively (Britan et al., 2007). Using single-phase approach, Britan et al. developed a full numerical solution to predict the diffusion pressure of gas filtration through dense granular media while providing a scaling procedure between pressure profiles arising from different combinations of granular media and incident shock (Britan et al., 2006). In the scenario involving intensified shock and loosely packed particles, the compaction of particles becomes nontrivial so that the assumption of the rigid solid skeleton no longer holds. In addition, gas temperatures in the wake of the reflected shock markedly rises; therefore, it is inappropriate to assume that the gas temperature is equal to that of the solid granular material. To overcome these limitations, the two-phase approach incorporates the volume-averaged governing equations of the particle phase, which allows for the variation in porosity. Additionally, the interphase energy transfer is considered. To solve the macroscopic governing equations for separate phases, it is necessary to derive some complementary closures, which is challenging because the constitutive relation of the particle phase with vastly varying porosities is still lacking. Therefore, in most cases, the velocity of the particle phase and the porosity variation are either assumed to be negligible or imposed from experimental measurements (Eriksen et al., 2018). Thus, we barely consider the spontaneous evolution of diffusion pressure, which is strongly affected by the coupling between gas filtration and particle compaction.

Instead of describing the particle phase as a continuum material, the discrete element method (DEM) tracks individual particles and accounts for interparticle contact/collision. The evolution of the solid skeleton is the result of collective particle motions. Coupling compressible computational fluid mechanics and DEM, referred to as CMP-PIC in our proposed previous publications, allows us to model the emergent shock compaction of mobile particles alongside transient gas flows (Tian et al., 2020). Numerical studies reveal the profile transition of diffusion pressure corresponding to the development of the compaction front. A shoulder in the monotonically decaying pressure profile emerges at the compaction front, upon which the gas velocity is in balance with that of the compacted particles. The deflection of the pressure at the compaction front can also be reproduced by the single-phase approach combined with the imposed compaction front conditions. Because the single-phase approach does not consider the width of the compaction front, which arises from the discreteness of granular media, it cannot properly account for the pressure distribution beyond the compaction front. The deviation between the pressure profiles derived from CMP-PIC simulations and the single-phase approach becomes significant as the effective Reynold number, Re_f, increases. Correspondingly, the non-isothermal effect becomes appreciable and leads to a higher shoulder pressure than that predicted by the isothermal single-phase approach. The non-isothermal effect is manifested in the theoretical model of the shoulder pressure, which also depends on the initial porosity.

Brief accounts of CMP-PIC and the single-phase approach will now be presented in Section 2. The numerical setup is shown in Section 3. The dynamic compaction of shock-loaded mobile particle columns with varying porosities is described in Section 4.1. The corresponding pressure evolution is analysed in Section 4.2. We reveal the coupling between the shock compaction and the build-up of the diffusion pressure and proceed to propose the prediction model of the shoulder pressure. The shock compaction and the non-isothermal effect also contribute to the profile transition of the transient velocity, as shown in Section 4.3. The density and temperature profiles associated with gas filtration are introduced in Section 4.4. The influence of unsteady flows at the upstream surface is discussed in Section 5. A brief summary is given in Section 6.

2. Method

2.1. CMP-PIC

Numerical simulations were performed based on CMP-PIC, a coarse-grained Euler–Lagrange approach suitable for gas-particle flows in laboratory-scale systems (Koneru et al., 2020; Sundaresan et al., 2018). The CMP-PIC approach tracks and accounts for contact interactions between parcels. Each parcel consists of multiple individual particles with the same physical and kinetic properties. The number of real particles that constitute a computational parcel is quantified using a scaling factor called the super particle loading, α^2, whose value is set based on the volume/mass fraction of the particles and computational memory available. For particle-gas systems, the reported α^2 in previous literature ranges from $O(10^1)$ to $O(10^3)$ (Koneru et al., 2020; Osnes et al., 2017; Xue et al., 2020). In this study, α^2 is on the order of $O(10^1)$.

For the gas phase, the volume-averaged governing equations [Eqs. (1)–(3)] constructed in the Eulerian frame are based on a five-equation transport model, which is a simplified form of the Baer–Nunziato (B-N) model (Baer and Nunziato, 1986) that has been modified to consider compressible multiphase flows ranging from dilute to dense gas-particle flows (Carmouze et al., 2020; Chiapolino and Saurel, 2020):

$$\frac{\partial\left(\varepsilon\rho_f\right)}{\partial t}+\nabla\cdot\left(\varepsilon\rho_f\mathbf{u}_f\right)=0 \tag{1}$$

$$\begin{aligned}\frac{\partial\left(\varepsilon\rho_f\mathbf{u}_f\right)}{\partial t}&+\nabla\cdot\left(\varepsilon\rho_f\mathbf{u}_f\mathbf{u}_f\right)+\nabla\left(\varepsilon P_f\right)\\&=P_f\nabla\varepsilon+\sum_i\left\{(1-\varepsilon_{p,i})\rho_{p,i}D_{p,i}\left(\mathbf{u}_{p,i}-\bar{\mathbf{u}}_f\right)\right\}\end{aligned} \tag{2}$$

$$\begin{aligned}\frac{\partial\left(\varepsilon\rho_f E_f\right)}{\partial t}&+\nabla\cdot\left(\varepsilon\rho_f E_f\boldsymbol{u}_f+\varepsilon P_f\boldsymbol{u}_f\right)=P_f\nabla\varepsilon\cdot\bar{\mathbf{u}}_p\\&+\sum_i\left\{(1-\varepsilon_{p,i})\rho_{p,i}D_{p,i}\left(\mathbf{u}_{p,i}-\bar{\mathbf{u}}_f\right)\cdot\mathbf{u}_{p,i}\right\}\end{aligned} \tag{3}$$

The volume fraction of the gas phase (i.e., porosity) is expressed by ε. The velocity, density, pressure, and total energy of the gas flow are represented by $\mathbf{u}_f$, ρ_f, P_f and E_f, respectively. $E_f=\rho_f e_f+0.5\,\rho_f\mathbf{u}_f\mathbf{u}_f$, where e_f is the specific internal energy. $\rho_{p,i}$ and $\mathbf{u}_{p,i}$ are the density and velocity of parcel i, $D_{p,i}$ is the drag force coefficient of parcel i. $\varepsilon_{p,i}$ is the local porosity of parcel i. $\bar{\mathbf{u}}_f$ is the average fluid velocity at the location of parcel i, $\bar{\mathbf{u}}_p$ is the average parcel velocity over the fluid cell. It is noteworthy that the first term on the right-hand side of Eq. (2), $P_f\nabla\varepsilon$, is the nozzling term that becomes significant wherever the porosity gradient is non-trivial.

We use the D_i Felice model combined with Ergun's equation to calculate D_p, which is essentially a nonlinear drag force model (Di Felice, 1994). The D_i Felice model combined with Ergun's equation (Ergun, 1952), which considers the effects of both the particle Reynold number, Re_p, and the porosity, ε, has been widely used in

particle-laden multiphase flows. D_p is a function of Re_p and ε:

$$D_{p,i} = \frac{3}{8sg} C_d \frac{\left|\mathbf{u}_f - \mathbf{u}_{p,i}\right|}{r_p} \tag{4}$$

$$C_d = \frac{24}{Re_p} \begin{cases} 8.33\dfrac{1-\varepsilon}{\varepsilon} + 0.0972 Re_p & \text{if } \varepsilon < 0.8 \\ f_{base} \cdot \varepsilon^{-\zeta} & \text{if } \varepsilon \geq 0.8 \end{cases} \tag{5}$$

$$f_{base} = \begin{cases} 1 + 0.167 Re_p^{0.687} & \text{if } Re_p < 1000 \\ 0.0183 Re_p & \text{if } Re_p \geq 1000 \end{cases} \tag{6}$$

$$\zeta = 3.7 - 0.65 \exp\left[-\frac{1}{2}(1.5 - \log_{10} Re_p)^2 \right] \tag{7}$$

where C_d is the dimensionless coefficient of the drag force; sg is the specific weight of individual particles, where $sg = \rho_p/\rho_f$; and r_p is the particle radius. For dense particle flows ($\varepsilon < 0.8$), Eq. (4) reduces to the original Ergun equation. Otherwise, C_d takes the form of Stokes's law multiplied by a factor of f_{base}, which varies with Re_p, as indicated by Eqs. (6) and (7).

The particle phase is represented by discrete parcels whose motion is governed by Newton's second law [Eqs. (8) and (9)]:

$$\frac{d\mathbf{u}_{p,i}}{dt} = D_{p,i}\left(\bar{\mathbf{u}}_f - \mathbf{u}_{p,i}\right) - \frac{1}{\rho_p}\nabla P_f + \frac{1}{m_p}\sum_j \mathbf{F}_{C,ij} \tag{8}$$

$$\frac{d\mathbf{x}_{p,i}}{dt} = \mathbf{u}_{p,i} \tag{9}$$

where $\mathbf{u}_{p,i}$ and $\mathbf{x}_{p,i}$ denote the velocity and displacement of parcel i, respectively; m_p represents the mass of the parcel and $\mathbf{F}_{C,ij}$ represents the collision force between parcels i and j.

A four-way coupling strategy (Ukai et al., 2010) was adopted to account for the momentum and energy transfer between gases and particles. Specifically, the drag force and the associated work from particles were incorporated into the momentum [Eq. (2)] and energy [Eq. (3)] equations of the gas phase as the source terms. The parcels are driven by the pressure gradient force, drag force, and collision force between themselves [Eq. (8)]. A soft sphere model, represented by a coupling spring and dashpot, was used to model the collision force between parcels (Apte et al., 2003). $\mathbf{F}_{C,ij}$ thus consists of a repulsive force and a damping force:

$$\mathbf{F}_{C,ij} = k_{n,p}\boldsymbol{\delta}_n - \gamma_{n,p}\mathbf{u}_{n,ij} \tag{10}$$

where $k_{n,p}$ and $\gamma_{n,p}$ are the stiffness and damping coefficients of parcels, and $\boldsymbol{\delta}_n$ and $\mathbf{u}_{n,ij}$ are the overlap and normal velocity difference between parcels in contact. $\gamma_{n,p}$ is a function of the parcel restitution coefficient ε_p (Crowe et al., 2012):

$$\gamma_{n,p} = -\frac{2\ln\varepsilon_p}{\sqrt{\pi^2 + \ln\varepsilon_p}}\sqrt{m_{p,ij}k_{n,p}}$$
$$m_{p,ij} = \sqrt{m_{p,i}m_{p,j}/(m_{p,i} + m_{p,j})} \tag{11}$$

To solve the equations governing the gases, the weighted essentially non-oscillatory (WENO) (Liu et al., 1994) scheme was used to reconstruct the primary flow variables. A Riemann solver proposed by Harten, Lax, and van Leer (Toro, 2009) was used to obtain the intercell fluxes. The third-order Runge–Kutta method was applied for the time integration. The equations describing the parcel velocity and position were discretized by the velocity-Verlet algorithm (Kruggel-Emden et al., 2008). Bilinear/trilinear interpolation functions were used to calculate the particle volume fraction and source terms on the Eulerian grids, as well as the fluid variables on Lagrangian parcels. Numerical details with regard to CMP-PIC are provided in the literature (Li et al., 2021; Meng et al., 2019; Tian et al., 2020; Xue et al., 2020).

The present CMP-PIC framework has been validated against Rogue's experiments involving shock waves propagating through particle curtains (Tian et al., 2020), shock tube experiments wherein particle columns are impinged head-on by incident shocks (Tian et al., 2020), and shock dispersion of particle rings (Xue et al., 2020). Fig. 1 shows a comparison of the experimentally and numerically derived gaseous overpressure histories, $\Delta P_f(t)$, registered upstream of and inside a granular column impinged by an incident shock wave with a Mach number $M_s = 1.41$ (van der Grinten et al., 1985). The simulation was performed on a three-dimensional configuration (see Fig. 1(a)) wherein a particle column with a volume fraction of $\varphi_0 = 0.7$ consists of spherical fixed particles with an average diameter of $d_p = 0.375$ mm, consistent with the experiment. A good agreement between the simulation results and the experimental measurements corroborates the reliability of CMP-PIC in reproducing the shock-induced transient gas flow through porous media. The pressure signal measurements shown in Fig. 1(b) comprise contributions from both the viscous and inertial resistances; thus, it is necessary to use the nonlinear drag coefficient model in simulations.

2.2. Single-phase approach combined with shock compaction

The single-phase approach presented in this study is similar to Morrison's approach to the problem of gas infiltration (Morrison, 1972). The evolution of interstitial gas pressure P_f inside the granular medium with porosity $\varepsilon = 1-\varphi_p$ and velocity u_p is given by the equation:

$$\frac{\partial\left(\varepsilon P_f\right)}{\partial t} = \frac{1}{\mu}\frac{\partial}{\partial x}\left(kP_f\frac{\partial P_f}{\partial x}\right) + \frac{\partial\left[\varepsilon P_f \mathbf{u}_p\right]}{\partial x} \tag{12}$$

where μ is the interstitial gas viscosity and k is the permeability of the medium. For a granular medium composed of spherical granules, k is a function of the particle diameter, d_p; and the granular medium porosity, ε, through the following relation:

$$k = \frac{1}{150}\frac{\varepsilon^3}{(1-\varepsilon)^2}d_p^2 \tag{13}$$

For the granular column composed of loosely packed mobile particles, upon shock impingement, a compaction front (CF) begins to traverse the particle layers at the velocity of V_{CF}, across which the volume fraction jumps from φ_0 to the maximum value φ_{comp}, as illustrated in Fig. 2(a). The compacted particles in the wake of the CF gain the velocity of $u_{p,comp}$. Similarly, the upstream front of the granular column moves at the velocity of $u_{p,comp}$. To properly couple the gas infiltration with the dynamic particle compaction, we attached the reference frame with the upstream front of the granular column so that u_p in Eq. (12) equals zero for the compacted particles and is replaced by $-u_{p,comp}$ for the uncompacted particles. The CF propagates at velocity $V_{CF}-u_{p,comp}$ with respect to the new reference frame. The newly introduced variables, $u_{p,\,comp}$ and V_{CF}, must be correlated with the properties of the granular medium and the shock intensity. In literature (Li et al., 2021), we deduced the expressions for $u_{p,\,comp}$ and V_{CF} based on the momentum equation combined with the Rankine-Hugoniot condition across the CF:

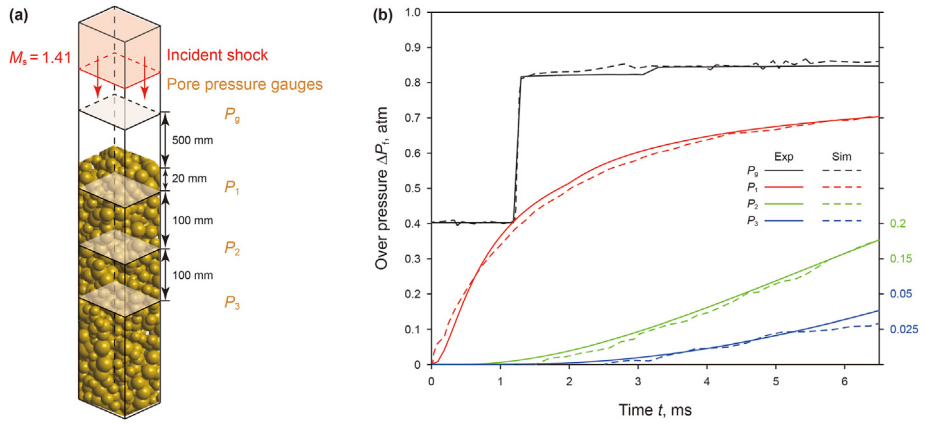

Fig. 1. Pressure signals at four different locations of an air-filled porous medium. Solid lines: experiment; dashed lines: CMP-PIC calculations.

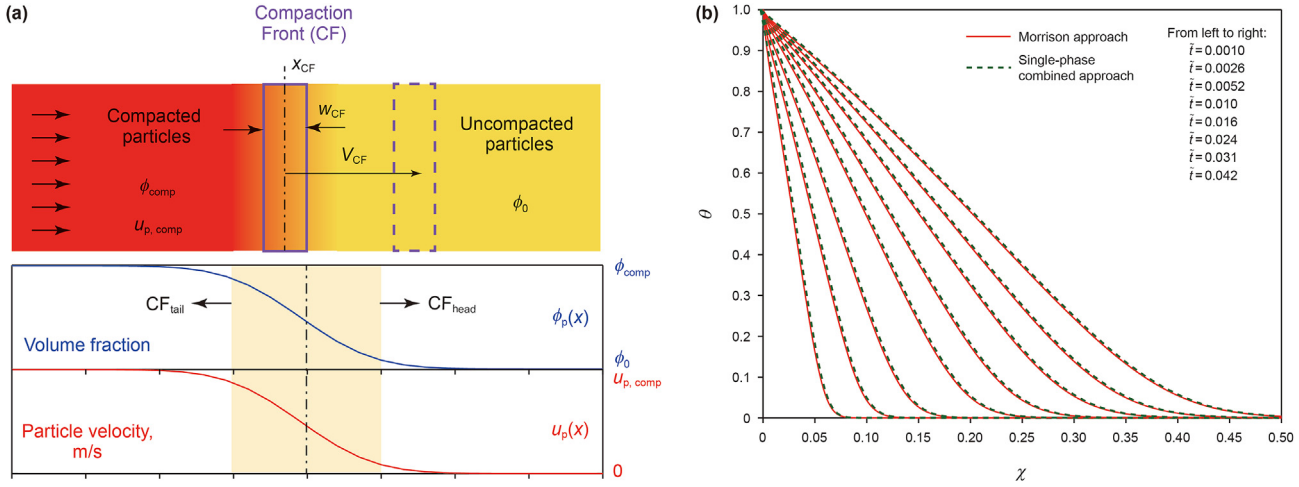

Fig. 2. Profiles of diffusing pressure inside the granular column with the rigid solid skeleton. Solid and dashed lines represent the analytical solutions given by Morrison's approach and the numerical solution based on Eq. (12).

$$u_{p,comp} = \sqrt{\frac{(P_r - P_0)}{\rho_p}\frac{\varphi_{comp} - \varphi_0}{\varphi_0 \varphi_{comp}}} \tag{14}$$

$$V_{CF} == \sqrt{\frac{(P_r - P_0)}{\rho_p}\frac{\varphi_{comp}}{\varphi_0(\varphi_{comp} - \varphi_0)}} \tag{15}$$

where P_r is the reflected pressure at the upstream front of the granular column and ρ_p is the density of the particle material. For granular columns with a typical $\varphi_0 \geq 0.4$, the shock reflection off the upstream surface riddled with fine pores approximates that off the solid surface (Skews, 2001). Thus, P_r is a function of the Mach number of the incident shock, M_s:

$$P_r = \frac{\left[2\gamma {M_s}^2 - (\gamma - 1)\right]\left[(3\gamma - 1){M_s}^2 - 2(\gamma - 1)\right]}{(\gamma + 1)\left[(\gamma - 1){M_s}^2 + 2\right]} P_0 \tag{16}$$

Considering a steady boundary condition, the upstream surface of a semi-infinite granular column is subject to a constant pressure, $P_f\ (x = 0) = P_r$. Although the gaseous temperature and density would immediately jump alongside P_f upon shock reflection, we still assume an isothermal gas flow; therefore, the gas temperature T_f is consistent with that of particles, $T_f = T_p = T_{amb}$. The gas density ρ_f varies with the pressure P_f, $\rho_f = P_f/RT_{amb}$, where R is the specific gas constant.

To avoid numerical oscillation across the CF, instead of using a Heaviside function, we use the Gauss error function as presented in Eq. (17) to approximate the porosity and particle velocity discontinuities across the CF:

$$\mathrm{erf}(x) = \frac{2}{\sqrt{\pi}}\int_0^x e^{-\eta^2} \mathrm{d}\eta \tag{17}$$

The φ_p and u_p gradually change from the compacted to the uncompacted state across the CF with a finite thickness of w_{CF}:

$$\varphi_p(x) = \frac{\varphi_{comp} - \varphi_0}{2} \cdot \mathrm{erf}\left(4 \cdot \frac{x - x_{CF}}{w_{CF}}\right) + \frac{\varphi_{comp} + \varphi_0}{2} \tag{18}$$

$$u_p(x) = -\frac{u_{p,comp}}{2} \cdot \mathrm{erf}\left(4 \cdot \frac{x - x_{CF}}{w_{CF}}\right) + \frac{u_{p,comp}}{2} \tag{19}$$

where x_{CF} is the distance of the CF from the upstream surface of the granular column, and $x_{CF} = (V_{CF} - u_{comp}) \cdot t$. The variations in φ_p and u_p when approaching the CF are demonstrated in the inset of Fig. 2(a).

Appendix A elaborates the algorithm we used to numerically

solve Eq. (12) with the reference frame fixed on the upstream surface of the granular column. For a granular medium with a rigid solid skeleton, dynamic compaction does not exist; therefore, Eq. (12) is reduced to the conventional Darcy equation. The numerical solution yields rise to pressure diffusion identical to that derived from Morrison's approach, as indicated in Fig. 2(b). Note that the pressure diffusion profiles depicted in Fig. 2(b) represent the distribution of scaled pressure, $\theta = (P_f - P_0)/(P_r - P_0)$, over the scaled distance, $\chi = x/L$, where L is the length of the granular column. Each diffusing pressure profile corresponds to one specific instant denoted by the scaled time, $\tilde{t} = t/t_{sc}$, where the scaling factor for the time, $t_{sc} = L/V_{sc}$. The scaling factor for the velocity, V_{sc}, is:

$$V_{sc} = \frac{1}{150}\frac{P_5 - P_0}{L\mu}\frac{(1-\varphi_0)^2}{\varphi_0^2}d_p^2 \tag{20}$$

The same velocity and time scaling method is used throughout this study.

3. Numerical setup

A two-dimensional configuration illustrated in Fig. 3(a) was used to investigate the shock-induced pressure diffusion in shock-compacting granular media, wherein a planar incident shock impinges head on the upstream surface of a long granular column composed of mobile spherical particles. The region ahead of the incident shock and the intergrain pores are filled with ambient air, $P_0 = 1.0 \times 10^5$ Pa, $T_0 = 298$ K. Because the upstream and downstream boundaries are nonreflective, the pressure exerted on the upstream surface of the column is kept constant, maintaining consistency with the reflected pressure, P_r, described by Eq. (16).

The granular column domain was filled by computational parcels generated by the radius expansion algorithm. A population of parcels with artificially small radii that ensures no particle or wall overlap is randomly created within the specified volume. Then, all parcels are expanded until the specified particle size distribution and desired porosity are satisfied (Yan et al., 2009). The real particle has a diameter of 100 μm, while the diameter of the parcel uniformly ranges from 400 to 750 μm to avoid potential crystallization during shock compaction. The inset of Fig. 3(a) shows a close-up image of the initial particle packing with $\varphi_0 = 0.5$, wherein the particles are coloured by the parcel-scale particle volume fraction, $\varphi_{p,local}$, calculated using Voronoi tessellation. A random but homogenous arrangement of parcels is achieved regardless of the overall volume fraction.

The parameters used in this study are $M_s = 1.54$, $\varphi_0 = 0.5$, $d_p = 100$ μm, $\mu = 1.81 \times 10^{-5}$ Pa s, and $L = 0.5$ m.

Among the parameters that affect gas infiltration through granular media, the shock intensity manifested by M_s and the initial volume fraction, φ_0, play equally important roles in shock compaction, as indicated in Eqs. (14) and (15). Thus, we devised two groups of numerical experiments with varying M_s (Group_M_s) and φ_0 (Group_ φ_0) to assess the influences of these two parameters. Table 1 lists the parameters of numerical cases that are required in the single-phase modelling, wherein the initial permeability, k_0, is calculated by Eq. (13) with $d_p = 100$ μm. For clarity, the system is labelled by M_s and φ_0, C-M_s-φ_0. Note that the deviation of P_r from the normal reflected pressure, P_5, becomes increasingly discernible as φ_0 decreases from 0.65 to 0.4. The volume fraction of the shock-compacted particles, φ_{comp}, also decreases as the initial packing becomes increasingly looser and/or the shock intensity is reduced. Pertinent parameters other than those listed in Table 1 are held constant, including the density of particle material, where $\rho_p = 2500$ kg/m^3; the normal stiffness of contacts between parcels, where $k_n = 2.25 \times 10^7$ N/m; and the restitution coefficient, where $\varepsilon_p = 0.6$.

Notably, φ_0 and φ_{comp} used in this study are those in the equivalent 3D assemblies converted from the porosity correlation between the 2D and 3D packings proposed by Borchardt-Ott (2012):

$$\varepsilon_{3D} = 0.2595 + \frac{\varepsilon_{2D} - 0.0931}{0.2146 - 0.0931}(0.4760 - 0.2595) \tag{21}$$

The values in Eq. (21), 0.2595 (0.4760) and 0.0931 (0.2146), are associated with the states of maximum or minimum packing

Table 1
Parameters in numerical cases.

Group	Case name	M_s	P_r	φ_0	φ_{comp}	k_0 (10^{-12} m^2)
G_M_s	C-1.56-0.4	1.56	5.94	0.4	0.671	90
	C-1.56-0.45		5.98	0.45	0.673	54.77
	C-1.56-0.5		6.03	0.5	0.676	33.33
	C-1.56-0.55		6.06	0.55	0.678	20.08
	C-1.56-0.575		6.08	0.575	0.678	15.48
	C-1.56-0.6		6.10	0.6	0.679	11.85
	C-1.56-0.625		6.12	0.625	0.68	9.00
	C-1.56-0.65		6.14	0.65	0.681	6.77
G_M_s	C-2.04-0.5	2.04	15.00	0.5	0.707	33.33
	C-2.04-0.55		15.11	0.55	0.709	20.08
	C-2.04-0.575		15.17	0.575	0.711	15.48
	C-2.04-0.6		15.22	0.6	0.712	11.85
	C-2.04-0.625		15.28	0.625	0.712	9.00
	C-2.04-0.65		15.36	0.65	0.712	6.77
G_φ_0	C-1.56-0.5	1.56	6.03	0.5	0.676	33.33
	C-1.83-0.5	1.83	10.54		0.685	
	C-2.04-0.5	2.04	15.00		0.707	

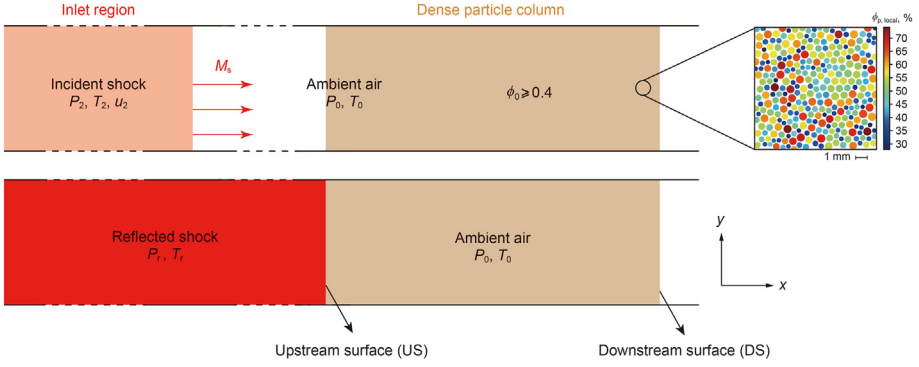

Fig. 3. Schematic diagram of the shock tube-based setup in the numerical experiments. The close-up image of initial particle packing coloured by the local particle volume fraction represents the case in which $\varphi_0 = 0.5$.

density in 2D (3D) packings composed of monodispersed spheres. This conversion correlation has been widely used to convert φ_{2D} to φ_{3D}, and vice versa. Accordingly, 3D particle volume fractions, φ_{3D} from 0.4 to 0.65, correspond to 2D particle volume fractions, φ_{2D} from 0.72 to 0.86. Considering the stochastic nature of the particle packing, each numerical experiment was performed on at least five realizations of granular columns to assess the variability in the results. The results presented thereafter are averaged over multiple realizations, while the error bars indicate the variability arising from the stochastic packing structures.

4. Results and analysis

4.1. Dynamics of shock compaction

Fig. 4 shows a snapshot of an initially uncompacted granular column in case C_1.56_0.5 a short time after shock impingement. By rendering images of the parcels coloured by their instantaneous velocity, $\tilde{u}_p$ (Fig. 4(a)), and parcel-scale volume fraction, φ_{local} (Fig. 4(b)), the microscopic details of the CF formation are shown. While parcels in the wake of the CF generally move with velocity u_{comp} and parcels far ahead are stationary, we find velocities over the entire range [0, u_{comp}] in a transition region centred at the CF. Specifically, many finger-like chains of particles percolate the width of the *CF*, causing roughness in the front. When we plot the coarse-grained velocity u_p vs. $\tilde{x} = x/d_p$ (Fig. 4(c)), however, these rough protrusions average into a smooth profile with a soft transition from $u_p = u_{comp}$ on the trailing edge of the CF (CF_{tail}) to $u_p = 0$ on the leading edge of the CF (CF_{head}). Similarly, the profile of the coarse-grained local volume fraction, $\varphi_{local}(\tilde{x})$, also shows a corresponding transition from φ_{comp} to φ_0, as shown in Fig. 4(d). The positions of CF_{tail} and CF_{head} are determined in such a way that u_p (and φ_{local}) reaches 95% and 5% values of u_{comp} (and φ_{comp}), respectively. At the position of CF, u_p (and φ_{local}) is the half value of u_{comp} (and φ_{comp}). The distance between CF_{tail} and CF_{head} yields a measurement of the CF's width, w_{CF}. The existence of a finite w_{CF} justifies the introduction of a Gauss error function to describe the variations of u_p and φ_{local} across the CF in the single-phase numerical solution. The evolution of the scaled CF width, $\tilde{w}_{CF} = w_{CF}/d_p$, is plotted in Fig. 4(e). After a short inception phase, $\tilde{w}_{CF}$ converges to a steady value, $\tilde{w}_{CF} = 15.3$, indicating the commencement of a steadily advancing CF. This period of time required to reach steady state is represented as $\tilde{t}_{st}$.

To describe when the compaction front becomes steady and changes of the steady-state width of it, Fig. 5(a) shows the relationship between nondimensional steady-state time $\tilde{t}_{st}$ as well as nondimensional steady-state width $\tilde{w}_{CF}$ and investigated parameters (initial packing fraction and shock intensity). Numerical cases with the same Mach number are represented by the same symbols. The solid and dashed lines are fitting curves of these cases at corresponding Mach numbers. As reported in previous studies, the steady-state width dramatically increases with increasing packing fraction (Waitukaitis et al., 2013), while the steady-state time reduces rapidly. A stronger incident shock shortens the steady-state time and leads to a sharper front. We not only focus on the width of the compaction front, but also its movement. The propagation velocity of the compaction front is prescribed in Eq. (15) and is deduced from the bulk particle velocity in Eq. (14). The consistency of the numerical results and prediction model is shown in Fig. 5(b), while the scaled $u_{p,comp}$, $\tilde{u}_{p,comp} = u_{p,comp}/\sqrt{(P_r - P_0)/\rho_p}$ and scaled V_{CF}, $\tilde{V}_{CF} = V_{CF}/\sqrt{(P_r - P_0)/\rho_p}$ points of our numerical cases comply with the analytical prediction curves.

4.2. Diffusing pressure field

Fig. 6(a) and (b) show the pressure diffusion in cases C-1.56-0.5 and C-1.56-0.65, respectively, manifested by profiles of the coarse-

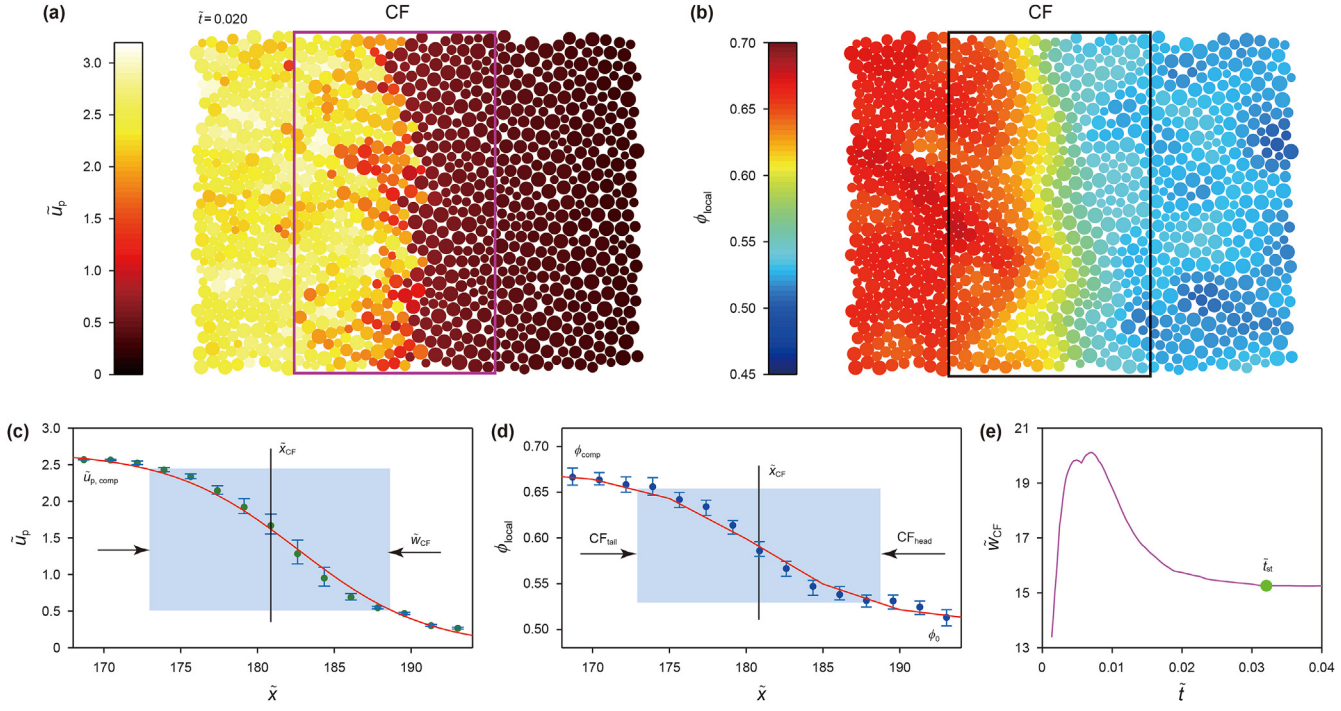

Fig. 4. The formation of CF in case C_1.56_0.5. (a) and (b) Close-up images near the CF coloured by the local particle volume fraction and nondimensional particle velocity. (c) and (d) The coarse-grained particle velocity and local volume fraction profiles. (e) The evolution of scaled CF width.

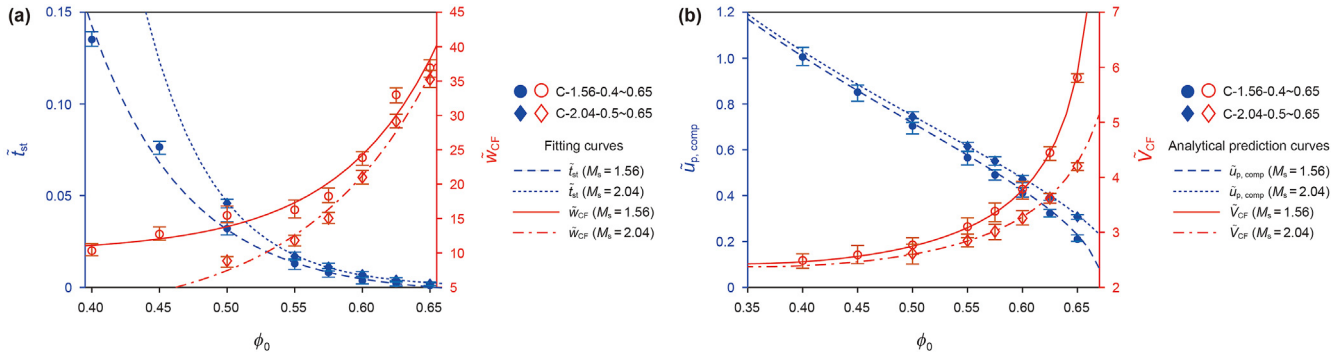

Fig. 5. (a) $\tilde{t}_{st}$ and $\tilde{w}_{CF}$ with φ_0 (b) The scaled $u_{p,comp}$ and V_{CF} with φ_0.

grained scaled pressure, $\theta(\tilde{x})$, of the simulated pressure fields as a function of depth into the granular column at different times $\tilde{t}$ after the shock impingement. For comparison, Fig. 6(c) and (d) present the respective single-phase numerical solutions. What is most striking is the shape transition of $\theta(\tilde{x})$ from a typical diffusion profile to a two-stage profile that undergoes substantial deflection upon the CF, more precisely the CF_{tail}. Inside the compacted particles, the $\theta(\tilde{x})$ profile exponentially decays from $\theta(\tilde{x}=0)=1$ at the upstream surface to a plateau pressure $\theta_{plateau}$ until approaching the CF_{tail}. Thereafter, $\theta(\tilde{x})$ dramatically decreases to the ambient pressure far ahead of the CF, $\theta(\tilde{x} \geq \tilde{x}_{CF_{head}}) = 0$. A close inspection of the CF formation (Fig. 4(e)) and pressure diffusion (Fig. 6(a)) reveals the correspondence between the CF formation and the profile transition of the diffusing pressure. The emergence of the CF results in the deflection of $\theta(\tilde{x})$ at the CF_{tail}. The deflection pressure, $\theta_{deflect}$, converges to $\theta_{plateau}$ at the end of the inception phase of the CF. The profile transition of $\theta(\tilde{x})$ also occurs in the single-phase numerical solutions, although the transition is nearly completed instantaneously, indicating that the numerical solutions indeed adequately account for the coupling between the shock compaction and the gas infiltration.

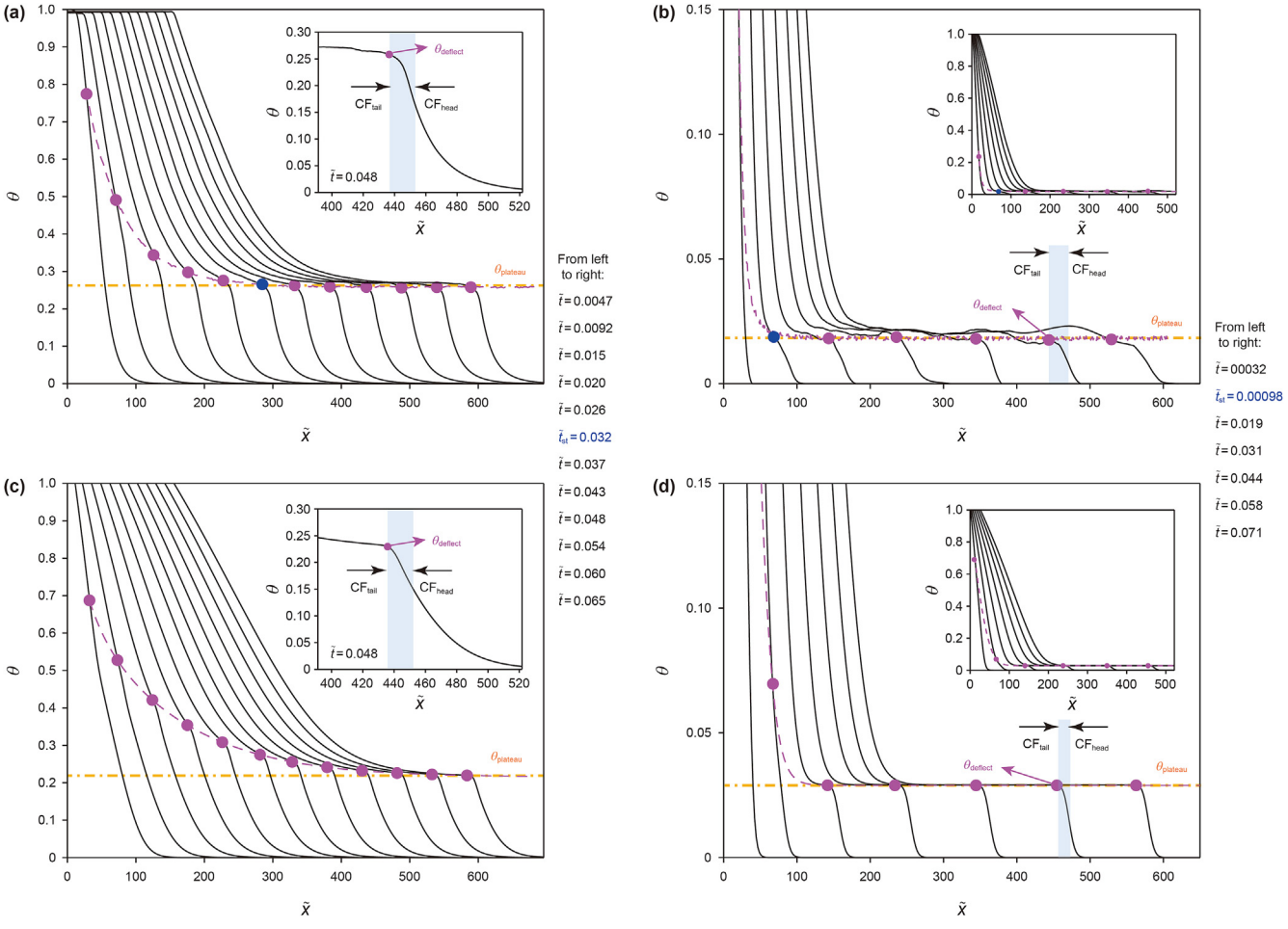

Fig. 6. The scaled pressure diffusion evolution by CMP-PIC (a) C-1.56-0.5 (b) C-1.56-0.65 and single-phase numerical solutions (c) C-1.56-0.5 (d) C-1.56-0.65.

The initial volume fraction, φ_0, strongly affects the $\theta_{plateau}$, as evident in Fig. 6. The dependence of $\theta_{plateau}$ on φ_0 is shown in Fig. 7, and a lower $\theta_{plateau}$ is observed in more densely packed granular columns. The dependence of $\theta_{plateau}$ on φ_0 can be understood in light of the Rankine-Hugoniot condition of the gaseous phase across the CF. Fig. 8 shows the evolution of the scaled gas velocity profile $\widetilde{u}_f = u_f/V_{sc}$ caused by pressure diffusion. Similar to the $\theta(\tilde{x})$ profiles, the $\widetilde{u}_f$ $(\tilde{x})$ profiles undergo a significant shape transition within the width of the CF, a prominent spike following the plateau of $\widetilde{u}_f$ that ends at CF_{tail}. With the steady advance of the CF, the amplitude of the velocity spike remains consistent, suggesting no net gas flow-in or flow-out within the thickness of the CF. With respect to the propagating CF, the mass continuity of the gaseous phase across the CF (see Fig. 9(a)) requires:

$$\varepsilon_{comp}\rho_{f,CF_{tail}}\left(V_{CF}-u_{f,CF_{tail}}\right)=\varepsilon_0\rho_0V_{CF} \tag{22}$$

where $\rho_{f,CF_{tail}}$ and $u_{f,CF_{tail}}$ are the gas density and velocity at CF_{tail}, respectively. In contrast, the interstitial gases at CF_{head} are barely disturbed so that $\rho_{f,CF_{head}}=\rho_0$, $u_{f,CF_{head}}=0$. During the steady shock compaction phase, except for the portion near the upstream surface, the compacted particles are markedly subjected to a uniform pressure field leading to a negligible pressure gradient force, $F_{\nabla P}$, as indicated in Fig. 6. The pressure plateau suggests minimum interstitial gas velocity relative to the particles in this study, thereby $u_{f,CF_{tail}}=u_{comp}$. The pressure plateau and the resulting velocity equilibrium between particles and interstitial gas in the wake of the CF_{head} are necessary for achieving a steady state of shock compaction. As illustrated in Fig. 9(b), if the pressure profile slopes downwards all the way into the CF_{head}, a velocity difference exists between particles and interstitial gases at the CF_{head}, which scales with the pressure gradient, $\Delta u = u_f - u_{comp} \sim (\partial P_f/\partial x)CF_{tail}$. As the length of the compacted pack increases, the slope of the pressure profile becomes gentler, reducing the velocity difference Δu. Because u_{comp} remains consistent, u_f decreases over time, which is contrary to the self-similar velocity profile across the thickness of the CF required by the steady state.

Considering the velocity equilibrium, $u_{f,CF_{tail}}=u_{comp}$, and replacing $\rho_{f,CF_{tail}}$ (and ρ_0) with $P_{f,CF_{tail}}$ (and P_0) using the ideal gas EOS, Eq. (22) yield the expression of $P_{f,CF_{tail}}$:

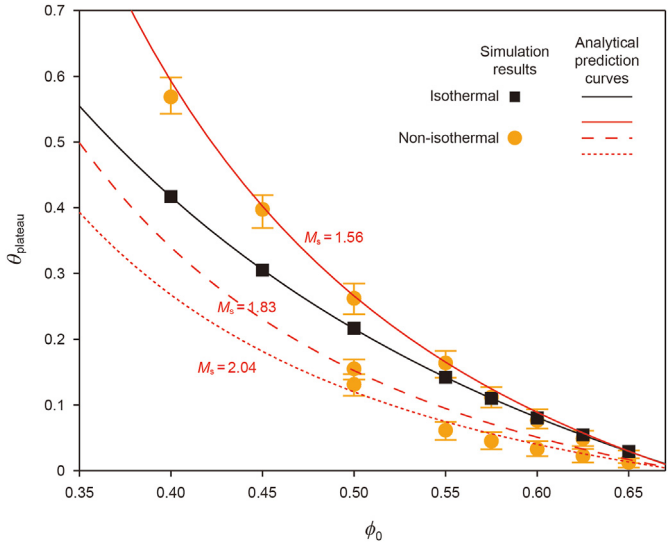

Fig. 7. The dependence of $\theta_{plateau}$ on φ_0. Solid circular symbols: CMP-PIC simulations, solid square: single-phase numerical solution, red line: non-isothermal predictions, black line: isothermal predictions.

$$P_{f,CF_{tail}}=\frac{V_{CF}}{V_{CF}-u_{comp}}\frac{1-\varphi_0}{1-\varphi_{comp}}\frac{T_{f,CF_{tail}}}{T_0}P_0 \tag{23}$$

Substituting Eqs. (14) and (15) into (23), the scaled pressure plateau $\theta_{plateau}$ can be expressed as:

$$\theta_{plateau}=\frac{P_{f,CF_{tail}}-P_0}{P_r-P_0}=\left[\frac{(1-\varphi_0)\varphi_{comp}}{(1-\varphi_{comp})\varphi_0}\frac{T_{f,CF_{tail}}}{T_0}-1\right]\frac{P_0}{P_r-P_0} \tag{24}$$

The Mach number dependence of $\theta_{plateau}$ is implicitly manifested by the temperature ratio $T_{f,CF_{tail}}/T_0$, which is not considered in the gas infiltration models assuming isothermal gas flows. Fig. 7 presents the analytical predictions of $\theta_{plateau}$ as a function of φ_0 under the isothermal and non-isothermal assumptions, indicated by red and black curves, respectively. Solid square symbols representing the $\theta_{plateau}$ derived from the single-phase numerical solution, collapse onto the black isothermal curve, while solid circular symbols representing the $\theta_{plateau}$ derived from the CMP-PIC simulations, scatter in a narrow band centred around the corresponding red non-isothermal curves. Stronger incident shocks give rise to both $P_{f,CF_{tail}}$ and P_r, while a greater increase in P_r leads to a decline in the non-isothermal curves. Particularly towards the lower limit of φ_0, the non-isothermal curves elevate rapidly. Thus, the non-isothermal effect becomes nontrivial for loosely packed granular media subjected to stronger incident shocks. The $T_{f,CF_{tail}}$ used in the calculation of each non-isothermal curves is estimated by assuming a linearly declining $T_f(x)$ profile from T_r to T_0:

$$T_{f,CF_{tail}}=(T_r-T_0)\cdot\theta_{plateau}+T_0 \tag{25}$$

where $\theta_{plateau}$ is the isothermal value at the same initial packing fraction, T_r is the temperature at the upstream surface of the granular column caused by the shock reflection and can be calculated by:

$$T_r=\frac{\left[2(\gamma-1)M_s^2-(\gamma-3)\right]\left[(3\gamma-1)M_s^2-2(\gamma-1)\right]}{(\gamma+1)^2M_s^2}T_0 \tag{26}$$

A gas pressure precursor is long been reported to precede the compaction wave in shock-loaded porous media that moves with the same velocity as the compaction wave front, as shown in Fig. 10(a) (Britan and Ben-Dor, 2006; Michiru et al., 1996). Stronger compaction waves sustained in porous media with high porosities result in precursors with higher amplitudes. Specifically, for the polyurethane foams with a porosity $\varepsilon = 0.98$ subjected to the incident shock $M_s = 1.7$, the precursor comprises approximately half of the stress signal for the foam sample (Michiru et al., 1996). The amplitude of the pressure precursor markedly increases upon precursor reflection off the end-wall, giving rise to a gas pressure peak at the end-wall that is even higher than the P_r at the upstream surface. Regarding the origin of the pressure precursor, investigators speculated that the gas which initially filled the void between the particles was pushed forwards by the compaction wave towards the uncompressed granular medium and caused an initial shoulder in the stress curves. We can justify the emergence of the precursor in the light of the coupling between shock compaction and gas infiltration. The volume fraction gradient within the width of the CF results in the pressure gradient in this study due to the nozzling term in the momentum equation (Eq. (2)). The steeper the volume fraction gradient is, the sharper the leading edge of the pressure profile becomes, causing an enhanced

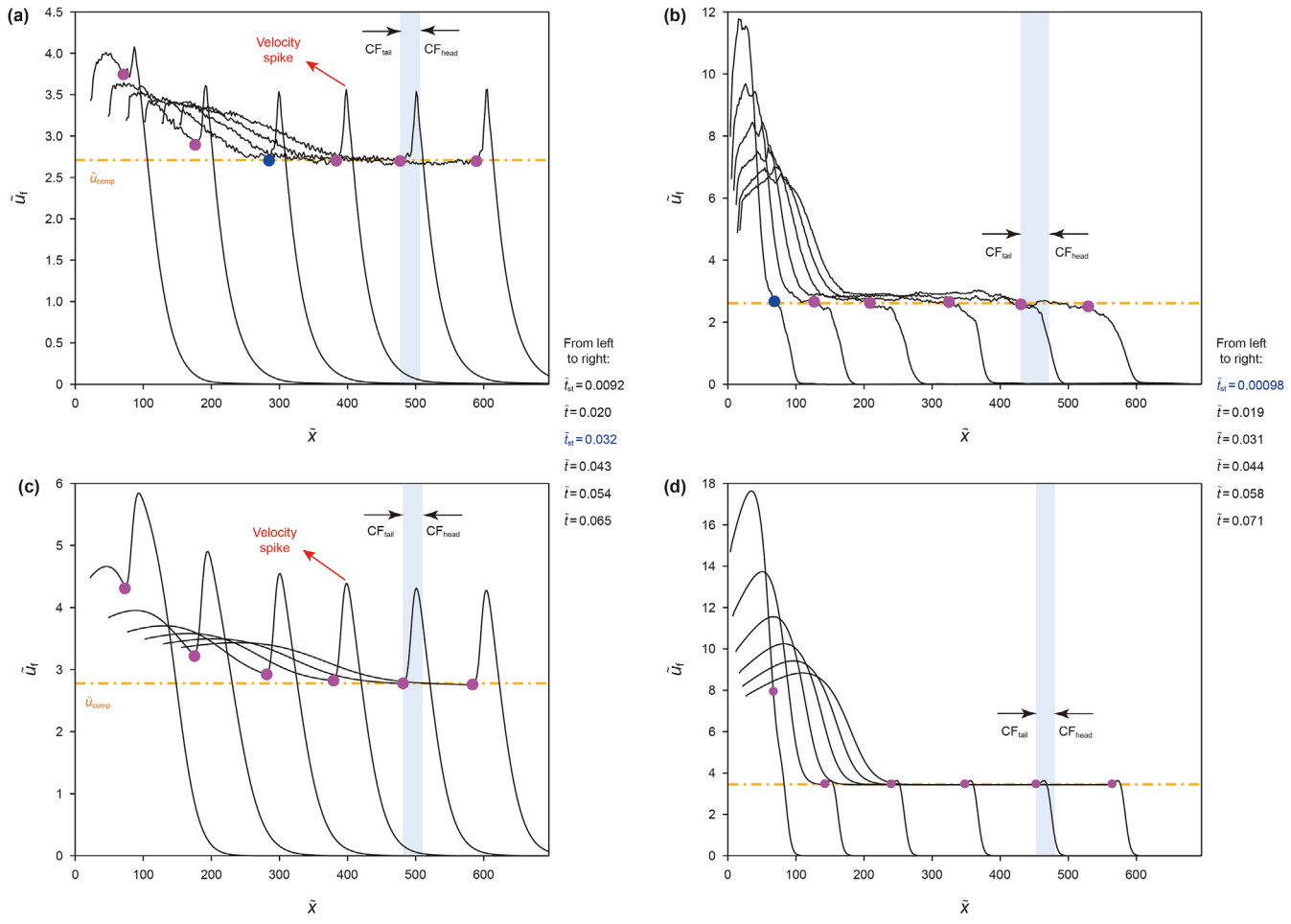

Fig. 8. The scaled gas velocity profiles by CMP-PIC (a) C-1.56-0.5 (b) C-1.56-0.65 and single-phase numerical solutions (c) C-1.56-0.5 (d) C-1.56-0.65.

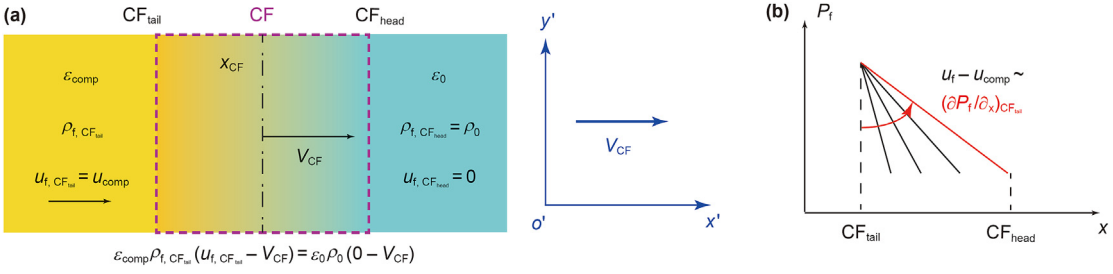

Fig. 9. (a) A schematic of the mass continuity of the gaseous phase across the CF (b) The relationship between the slopes of the pressure profile and the velocity difference.

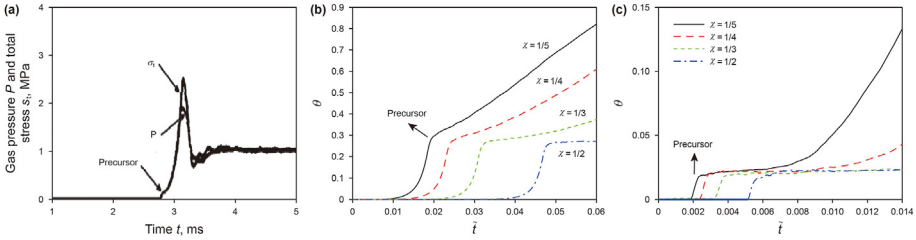

Fig. 10. The pressure histories and significant precursors at different distances from the upstream surface. (a) Britan's work, 2006 (b) C-1.56-0.5 (c) C-1.56-0.65.

pressure precursor. Fig. 10(b) shows the pressure histories at different distances from the upstream surface, highlighting significant precursors at the beginning of the pressure traces. In contrast, the much reduced volume fraction gradient across the width of the CF in the initially densely packed granular leads to a much gentler pressure slope, as shown in the close-up inset in Fig. 6(b). Therefore, the plateau pressure decreases with the initial volume fraction. The resulting pressure precursor becomes nearly negligible in the case C-1.56-0.65, as shown in Fig. 10(c).

4.3. Formation of velocity spike at the CF

The microscopic mechanism underlying the gas velocity spikes seen in Fig. 8(a) is illustrated in the close-up snapshot of the gas velocity field in regions moving with the CF, as shown in Fig. 11(a). Although the randomness of the particle arrangements is intrinsic to the particle packing, the local variations in volume fraction and particle velocity are most prominent across the thickness of the CF caused by finger-like chains of particles that carry the majority of the solid stresses (see Fig. 4(a) and (b)). As the interstitial gases travel through the thickness of the CF, the flow would be accelerated or decelerated as it navigates through the inhomogeneities brought by the "clustered" particle chains, forming micro gas jets. On average, the streamwise gas velocity surges as gases flow through the thickness of the CF. This mechanism, often referred to as the "nozzling" or the "channelling" effect, has been observed in particle-resolved simulations of blast-induced gas infiltration through particle beds. The nozzling effect attenuates as the gases flow through the CF_{head} into the uncompacted particles where the particle chains have not yet been formed. However, the micro gas jets persist well ahead of the CF_{head} and push the particles against each other. The ensuing collisions result in agglomeration and formation of long force chains of particles that are about to be compacted. With the aid of the micro gas jets, the roughness of the CF is amplified compared with that formed in other dynamic compaction with the absence of interstitial gas flows. Because the nozzling effect is strongly mitigated in the initially densely packed granular media where the particle agglomeration and the resulting inhomogeneities are suppressed, the interstitial gas flows become tempered with much weaker microjets, as shown in Fig. 11 (b). Therefore, in contrast with the distinctive velocity spike exhibited by the $\tilde{u}_f(\tilde{x})$ profiles in case C-1.56-50, we can barely detect noticeable spike in the $\tilde{u}_f(\tilde{x})$ profile in case C-1.56-60

The formation of the velocity spike can also be accounted for by the momentum balance of the interstitial gases as a continuous phase. With the reference frame fixed at the steadily propagating CF, the momentum equation of the interstitial gases becomes:

$$\frac{\partial\left(\varepsilon\rho_f u_f\left(u_f - V_{CF}\right)\right)}{\partial x} = F_{\nabla P} - F_{drag} \tag{27}$$

where $F_{\nabla P}$ and F_{drag} are the pressure gradient force [Eq. (28)] and the drag force [Eq. (29)] exerted on the interstitial gases inside the granular media with unit volume, respectively:

$$F_{\nabla P} = -\varepsilon\frac{\partial P_f}{\partial x} \tag{28}$$

$$F_{drag} = (1-\varepsilon)\cdot\left[150\left(\frac{1-\varepsilon}{\varepsilon}\right)^2\cdot\frac{1}{{d_p}^2}\mu\left(u_f - u_p\right) + 1.75\left(\frac{1-\varepsilon}{\varepsilon}\right)\frac{\rho_f\left(u_f - u_p\right)^2}{d_p}\right] \tag{29}$$

Due to the mass conservation of the interstitial gases, we have:

$$\frac{\partial\left[\varepsilon\rho_f\left(u_f - V_{CF}\right)\right]}{\partial x} = 0 \tag{30}$$

Thus, Eq. (27) becomes:

$$\varepsilon\rho_f\left(u_f - V_{CF}\right)\frac{\partial u_f}{\partial x} = F_{\nabla P} - F_{drag} \tag{31}$$

where $\varepsilon\rho_f(u_f - V_{CF})$ is unvaried throughout the granular column. Thus, the spatial variation in u_f depends on the difference between the magnitudes of $F_{\nabla P}$ and F_{drag}.

Fig. 12(a) and (b) show close-up images of the fields of $F_{\nabla P}$ and F_{drag} in the neighbourhood of the CF, respectively. Similar to the heterogeneous gas velocity field, the $F_{\nabla P}$ and F_{drag} fields also display particle-scale heterogeneities originating from particle agglomeration and micro gas jets. Further examination also indicates the strong pattern correlation between the $F_{\nabla P}$ and F_{drag} fields. Specifically, the same micro gas jets experience strong $F_{\nabla P}$ and F_{drag}. Those micro gas jets concentrate within the band between the CF and the

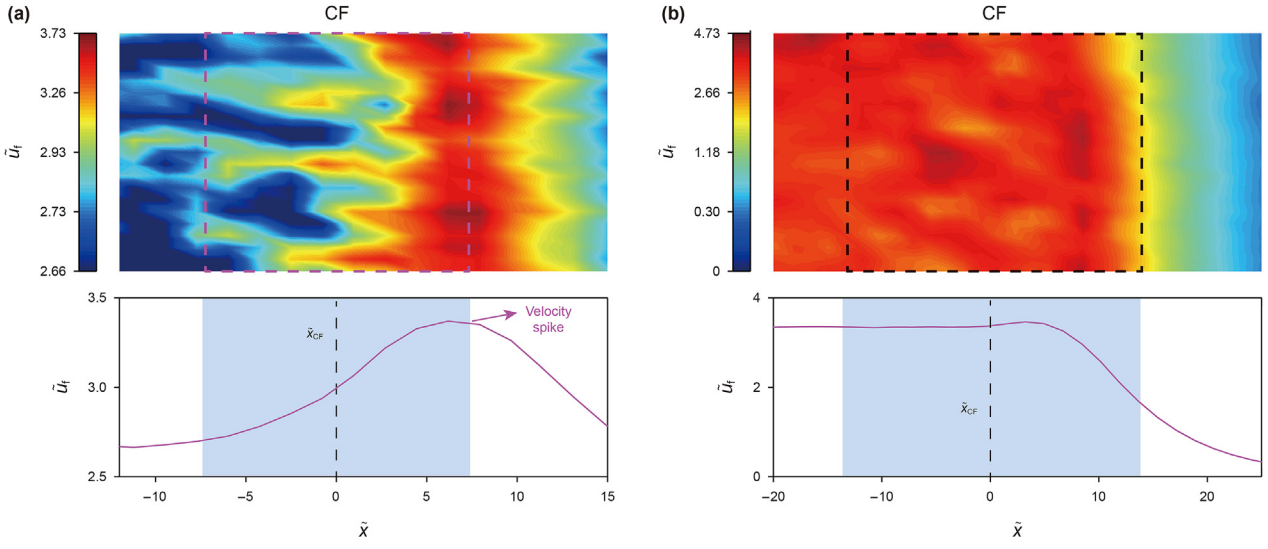

Fig. 11. Scaled gas velocity field and relative profile near the CF region. (a) C-1.56-50 (b) C-1.56-60.

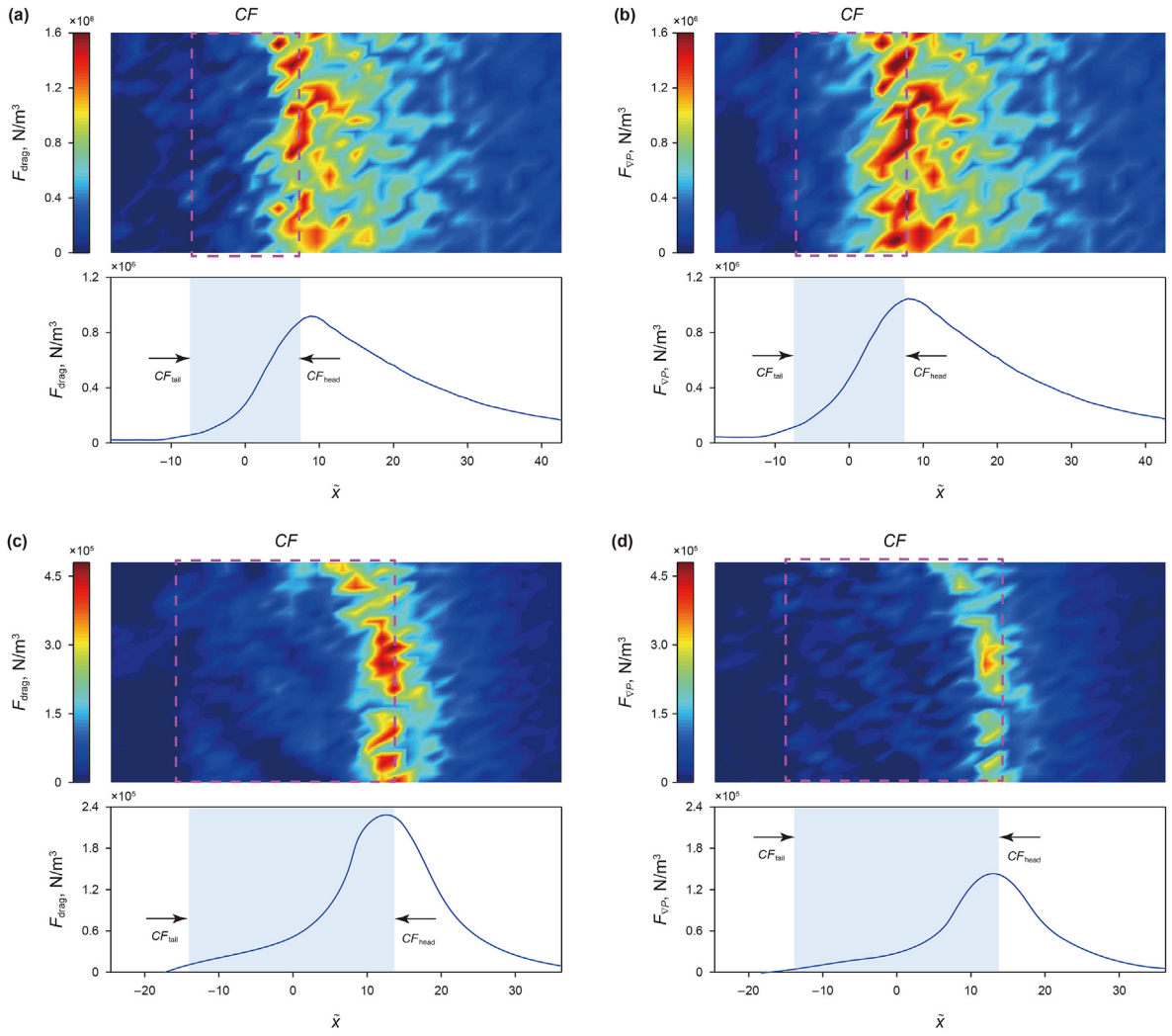

Fig. 12. F_{drag} and $F_{\nabla P}$ fields and relative profiles in the neighbourhood of the CF. (a) and (b) C-1.56-0.5. (c) and (d) C-1.56-0.6.

CF_{head} and disperse into the immediate region ahead of the CF_{head}, again consistent with the distribution of micro gas jets distinguishable in the velocity field, as shown in Fig. 11(a). The profiles of spanwise averaged $F_{\nabla P}$ and F_{drag}, $F_{\nabla P}(x)$ and $F_{drag}(x)$, reach their peaks at CF_{head} (see the bottom frames in Fig. 11(a) and (b)). The rising sides of $F_{\nabla P}(x)$ and $F_{drag}(x)$ result from the nozzling effect inside the width of the CF, while the declining slopes are indicative of the pressure diffusion in the uncompacted particles. The differences between $F_{\nabla P}(x)$ and $F_{drag}(x)$ are plotted in Fig. 13(a), which clearly shows a transition point at CF_{head}. Behind the CF_{head}, a surplus is found between absolute $F_{\nabla P}(x)$ and $F_{drag}(x)$, while beyond the CF_{head} $F_{drag}(x)$ exceeds $F_{\nabla P}(x)$. Accordingly, the gas flow accelerates all the way until it approaches CF_{head} and thereafter decelerates due to the stronger resistance.

The nozzling effect diminishes as the initial volume fraction of the granular column, φ_0, increases. In case C-1.56-0.6, the $F_{\nabla P}(x)$ and $F_{drag}(x)$ profiles level off far from the upstream surface and trail away beyond the CF_{head}, and any increases across the thickness of the CF are barely discernible, as shown in Fig. 11(c) and (d). The driving force of the interstitial gas flow, $F_{\nabla P}(x)$, is always smaller than the flow resistance, $F_{drag}(x)$, as shown in Fig. 13(b), causing the persistent deceleration of gas velocity through the width of the CF. Fig. 14 depicts the variation in amplitude of the scaled gas velocity spike, $\Delta\tilde{u}_{spike} = \left(u_{f,CF_{head}} - u_{f,CF_{tail}}\right)/u_{f,CF_{tail}}$, with increasing φ_0, where $u_{f,CF_{head}}$ and $u_{f,CF_{tail}}$ are the gas velocities at CF_{head} and CF_{tail}, respectively. $\Delta\tilde{u}_f$ becomes negligible when φ_0 is increased beyond a critical value, $\varphi_{0,cr}$, which decreases from 0.6 to 0.575 as M_s increases from 1.56 to 2.04. Compared with the φ_0 dependence of $\theta_{plateau}$, $\theta_{plateau}$ becomes minimized (i.e., $\theta_{plateau} < 0.08$). The two-stage pressure profile degenerates into the typical diffusing pressure profile with φ_0 higher than $\varphi_{0,cr}$. Thus, shock compaction tends to be decoupled from gas infiltration in initially densely packed granular media subjected to a strong incident shock.

As aforementioned the shape of the velocity spike depends on the volume fraction variation within the width of the CF, which changes with φ_0 and M_s. Since all the single-phase numerical solutions engage the same $\varphi_0(x)$ variation profile within the fixed width of the CF, which is steeper than the real $\varphi_0(x)$ profiles derived from the simulations in most cases, the velocity spikes produced in the numerical solution are more pronounced than those observed in the simulations and assume a negatively skewed shape rather than the positively skewed shape in simulations, as shown in Fig. 8(c) and (d).

The gas surge within the width of the CF brings about the dynamic gas pressure, which makes a significant contribution to the

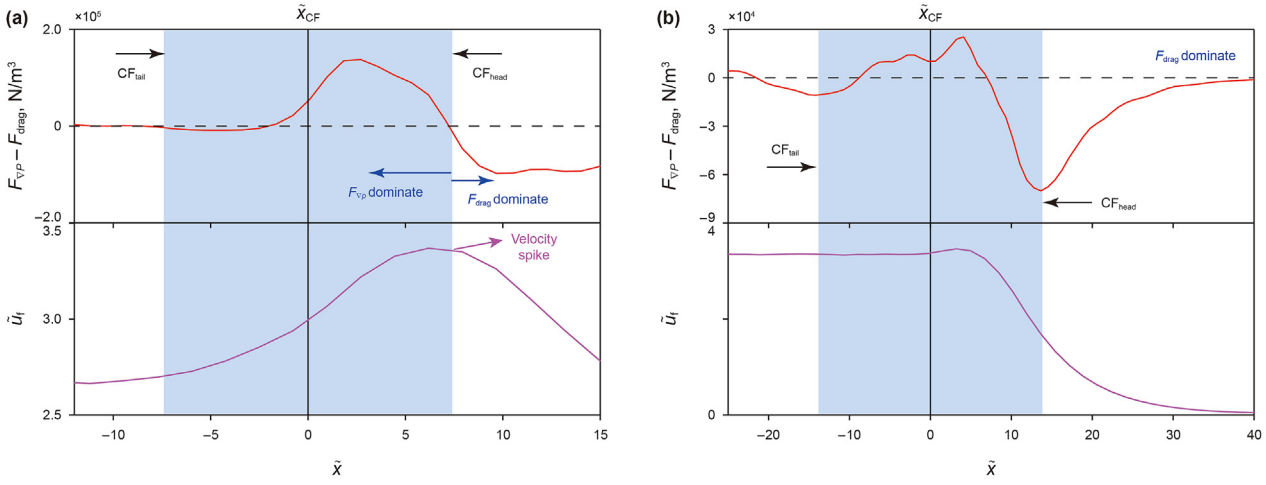

Fig. 13. The relationship between the differences in $F_{\nabla P}(x)$ and $F_{drag}(x)$ and the velocity spike. (a) C-1.56-0.5 (b) C-1.56-0.6.

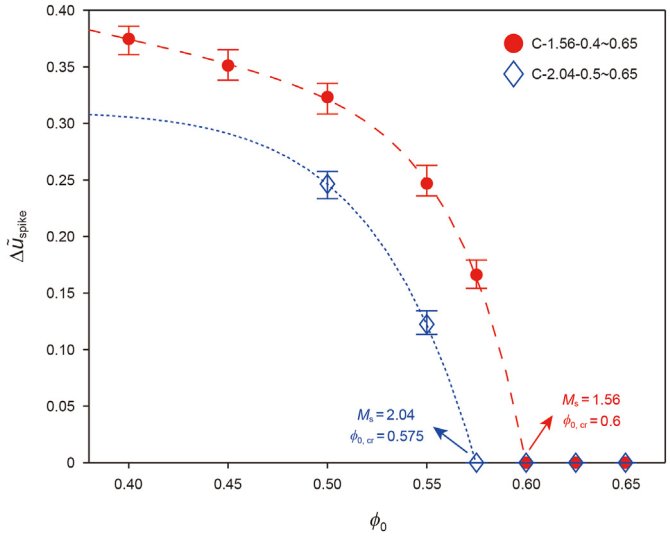

Fig. 14. The scaled gas velocity spike with increasing φ_0.

gas pressure precursor when the magnitude of the interstitial gas velocity is on the order of O(10^2) m/s, which is the case in porous media with high porosities (ε~0.9). In this scenario, properly estimating the gas peak velocity at CF_{head} as a function of φ_0 and M_s is necessary to predict the pressure precursor, which should be the focus of future research.

4.4. Profiles of thermodynamic variables

Fig. 15(a) and (b) depict the evolutions of the scaled temperature and density profiles in case C-1.56-0.5, where $\widetilde{T}_f = T_f/T_r$ and $\widetilde{\rho}_f = \rho_f/\sqrt{P_r/V_{sc}}$, where T_r is the gas temperature at the upstream surface. In contrast to the constant gas temperature assumed by the isothermal gas infiltration models, the $\widetilde{T}_f(\widetilde{x})$ profile exhibits distinctive features along the depth into the granular column. Specifically, a noticeable $\widetilde{T}_f$ peak is adjacent to the upstream surface, followed by multiple kinks in the portion throughout the compacted particles and a narrow spike across the width of the CF. For a steady coupling between the shock compaction and the gas infiltration signified by the constant u_{comp} and V_{CF}, the converged $\theta_{plateau}$, and self-similar profiles of the $\widetilde{u}_f$ and $\widetilde{T}_f$ spikes at different instants, the momentum balance of the interstitial gases requires a constant $\varepsilon\rho_f(u_f - V_{CF})$, or equivalently a constant $\varepsilon\ P_f/T_f\ (u_f - V_{CF})$ throughout the diffusion depth into the granular column. Thus, the variation in $\widetilde{T}_f$ is proportionate to the product of θ and $\widetilde{u}_f - \widetilde{V}_{CF}$. Considering the monotonic decaying $\theta(\tilde{x})$ profile and the constant $\widetilde{V}_{CF}$, it is the distinctive features in the $\widetilde{u}_f(\widetilde{x})$ profiles that result in the corresponding features in the $\theta(\tilde{x})$ profiles. Specifically, the velocity spike across the width of the CF if it exists causes the temperature spike in this study, as shown by the overlapping of the spikes of velocity and temperature (see the inset in Fig. 15(a)). Fig. 16 shows the dependence of the amplitude of the temperature spike, $\Delta\widetilde{T}_{spike} = \left(T_{spike} - T_{CF_{tail}}\right)/T_r$, on φ_0, where T_{spike} and $T_{CF_{tail}}$ are the sipke temperature and the gas temperature at the CF_{tail}, respectively. The correlation between $\Delta\widetilde{T}_{spike}$ and φ_0 resembles that between $\Delta\widetilde{u}_{spike}$ and φ_0. The characteristics in the $\widetilde{T}_f(\widetilde{x})$ profiles are also embodied in $\widetilde{\rho}_f(\widetilde{x})$ since $\rho_f = P_f/RT_f$. Specifically, the steep downstream facing decline side of the first temperature peak adjacent to the upstream surface produces a moderate increase in $\widetilde{\rho}_f$, as shown in the close-up plot in the inset of Fig. 15 (b). However, the temperature spikes across the width of the CF do not suffice to guarantee an increase in $\widetilde{\rho}_f$ so that the $\widetilde{\rho}_f(\widetilde{x})$ profiles from the CF_{tail} onwards primarily inherit the characteristics of the $\theta(\tilde{x})$ profiles. The $\widetilde{\rho}_f(\widetilde{x})$ curves deflect from the plateau at the CF_{tail} and proceed with a sharp slope into uncompacted particles ahead of the CF_{head}, as seen in the $\theta(\tilde{x})$ profiles.

5. Discussion

The shock-induced gas infiltration through the granular media may be influenced by the unsteady flows at the upstream surface. Specifically, Britan et al. identified the unsteady flow patterns inside a shock-loaded granular column induced by unsteady loading at the front surface of the column in shock tube experiments (Britan et al., 2007). Once the rarefaction wave reflected from the end-wall of the shock tube driver arrives at the front surface of the granular column, the total stress and the gas pressure quickly decrease, providing clear evidence that gas infiltration is an efficient tool in relieving the stresses inside the granular medium when it is subjected to a weak shock wave impact. They further developed a

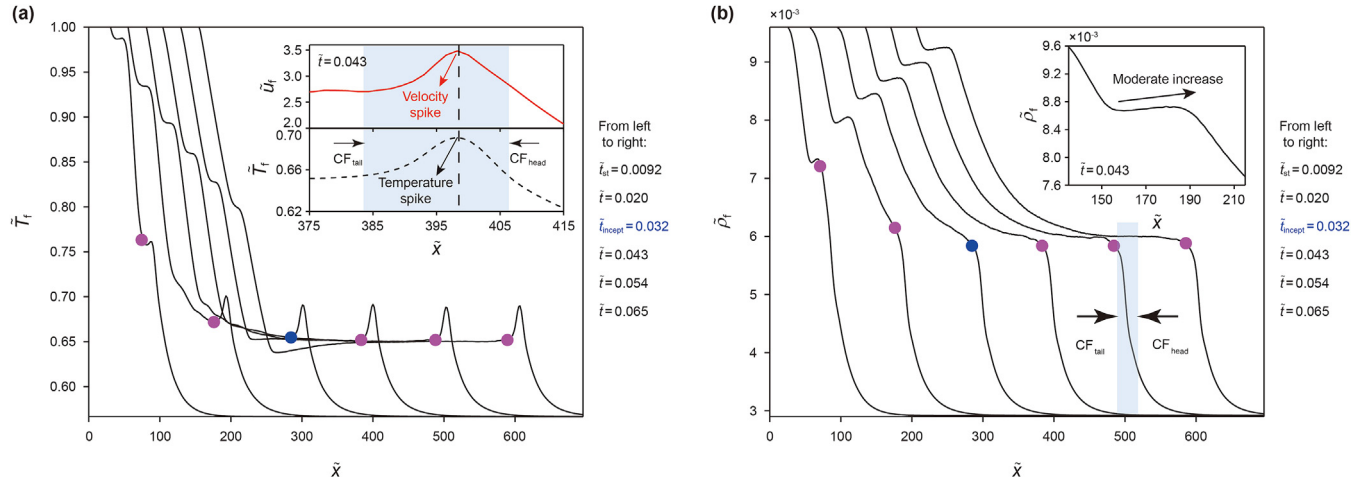

Fig. 15. The evolutions of (a) the scaled temperature and (b) the scaled density profiles in C-1.56-0.5.

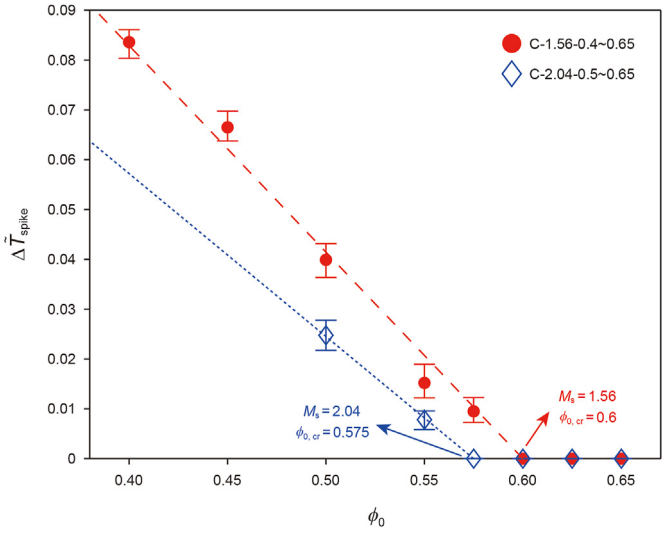

Fig. 16. The dependence of the scaled amplitude of the temperature spike $\Delta\tilde{T}_{spike}$ on φ_0.

general approach for predicting the pressure fields of unsteady gas flows through granular media, considering the unsteady boundary conditions (Britan et al., 2006). Their approach is similar to the single-phase numerical solution introduced in Section 2.2 but does not incorporate shock compaction.

In the CMP-PIC simulations performed in this study, the reflected back rarefaction wave is absent due to the nonreflective boundary conditions. The pressure history measured at the moving upstream surface, $P_{upstream}(t)$, also shows an initial unsteady phase, as shown in Fig. 17(a). Instead of an instantaneous pressure jump occurring at the normal shock reflection off the solid surface, $P_{upstream}(t)$ undergoes a substantial increase during a short period of time (t_{ini}~1 ms). Thereafter, $P_{upstream}(t)$ converges to a steady value, P_r, smaller than the reflected pressure resulting from the normal shock reflection, P_5. The initial increase phase of $P_{upstream}(t)$ arises from complex wave interactions ensuing the shock impingement. Fig. 18(a) presents the diagram of the wave structure after shock impingement upon the front surface of the rigid porous media first contemplated by Levy et al. (1993). The penetration of the transmitted shock wave through the front layer of the porous material can be viewed as a sharp front, a transmitted front, TF, which sweeps through the porous material while parts of it are reflected back as the reflected shock front, RS. As the TF progresses downstream, parts of it are left behind, bouncing back and forth inside the cavities of the pores. Some trapped transmitted fronts interact with each other, and some even find a way to emerge from the front edge of the porous material as weak compression waves, CW, which eventually catch up with the primary RS and increase the pressure field behind it. The emergence between the RS and a train of catching-up CWs results in a downstream adverse pressure and density gradient as well as a sloping down velocity profile in the wake of the RS, as shown in Fig. 17(b)–(d). The higher φ_0 is, the stronger the reflected compression waves become. Thus,

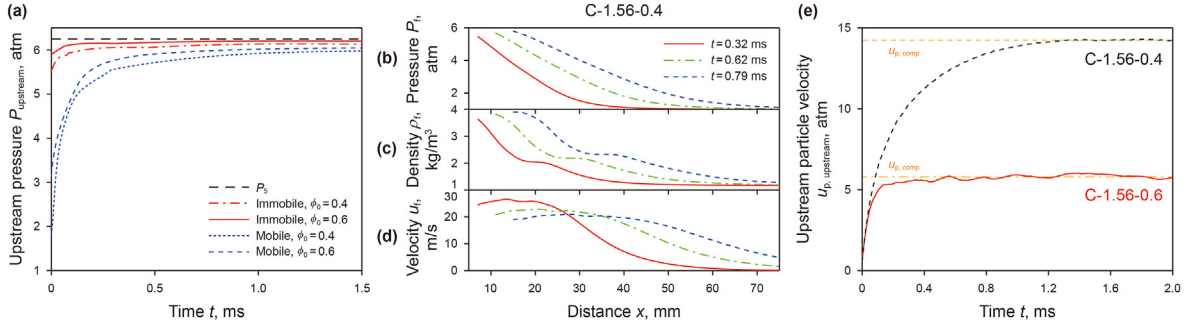

Fig. 17. (a) The pressure history measured at the moving upstream surface. (b)–(d) The profiles of pressure, density and gas velocity for case C-1.56-0.4. (e) History of the upstream surface velocity.

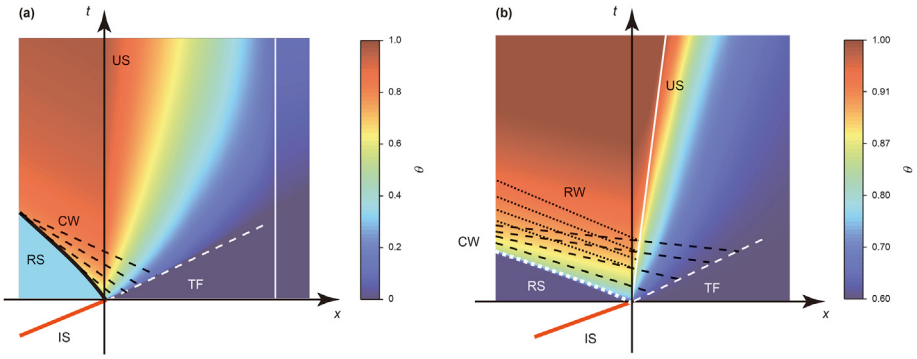

Fig. 18. Diagram of the wave structure after shock impingement on the upstream surface (US) of (a) immobile and (b) mobile porous media.

$P_{\mathrm{upstream}}(t)$ rises more rapidly in case C-1.56-0.6 than in case C-1.56-0.4 (see Fig. 17(a)). When penetrating the porous material, the TF becomes increasingly dispersed and eventually diminishes; thereafter, no more reflected compression waves are generated. This process ends earlier in granular columns with higher φ_0, as seen in Fig. 17 (a).

The build-up of $P_{\mathrm{upstream}}(t)$ is countered by the upstream travelling rarefaction waves, RW, issued from the accelerating upstream surface whose velocity converges to u_{comp} after a short period of acceleration, as plotted in Fig. 17(e). The rarefaction effects can be identified by comparing the $P_{\mathrm{upstream}}(t)$ curves of the mobile granular column and immobile one, as shown in Fig. 17(a). Without the rarefaction waves, P_{upstream} of the immobile one increases to a higher value than the mobile one. The deviation between them increases as φ_0 decreases because the acceleration of the upstream surface of the loosely packed granular column is more prominent.The counter effect brought by the accelerating upstream surface modifies the wave structure, as shown in Fig. 18(b).

Since we used relatively densely packed granular columns ($\varphi_0 \geq 0.4$) and particles with large inertia, the unsteady loading phase of P_{upstream} is insignificant in terms of the duration and the deviation of P_{r} from P_5. However, for porous media with high porosities ($\varepsilon > 0.9$) and light solid skeletons, the dissipation of the transmitted wave and the acceleration of the upstream surface both take much longer times so that the unsteady gas flows induced by the unsteady loading condition play a nontrivial role in the gas infiltration through the porous media.

6. Conclusion

In the present work, we describe the influence of the coupling between shock compaction and gas infiltration on pressure diffusion through a shock-loaded granular column via CMP-PIC and modified single-phase simulations. We first introduce the CMP-PIC method and propose a modified single-phase approach to investigate non-isothermal effect. A series of numerical experiments is conducted to assess the influence of shock intensity and initial volume fraction. The characteristics of the formed compaction front under shock-load are revealed. The compaction front maintains an unsteady state only for a short period of time, and its width does not change afterward. The formation of pressure deflection caused by shock compaction is manifested, and a prediction model for the steady deflection pressure is proposed. The non-isothermal effect on the steady pressure becomes increasingly significant as the incident shock strengthens and the initial volume fraction decreases. The nozzling effect, which originates from variations in local particle volume fraction, is discovered as a micro-mechanism for the deflection of the pressure profile as well as velocity and temperature spikes inside the width of the compaction front. A threshold of the initial volume fraction is also identified, beyond which the aforementioned spikes disappear while the difference in the competitive relationship between pressure gradient forces and drag forces becomes negligible. Finally, the scope of application is discussed in terms of the effects of interfacial motion and initial volume fraction on the pressure at the upstream surface.

Declaration of competing interest

The authors declare that they have no known competing financial interests or personal relationships that could have appeared to influence the work reported in this paper.

Acknowledgements

This work was supported by National Natural Science Foundation of China (Grants No. 11972088, No. 12122203).

Appendix A. Numerical solution algorithm for the combined single-phase approach

We attached the reference frame with the upstream front of the granular column, which simplifies the moving boundary problem into a fixed one. Eq. (12) becomes Eq. (A1) in this relative coordinate system:

$$\frac{\partial\left(\varepsilon P_{\mathrm{f}}\right)}{\partial t}=\frac{1}{\mu}\frac{\partial}{\partial x}\left(kP_{\mathrm{f}}\frac{\partial P_{\mathrm{f}}}{\partial x}\right)+\frac{\partial\left[\varepsilon P_{\mathrm{f}}\left(u_{\mathrm{p}}-u_{\mathrm{comp}}\right)\right]}{\partial x} \tag{A1}$$

To solve the model proposed in Eq. (A1), we first define a grid with $I+2$ nodes along the x-axis and $J+2$ nodes along the t-axis that has integer indices $i\in[0, I+1]$ and $j\in[0, J+1]$. Using a grid step size $\Delta x = 1$ mm, $\Delta t = 0.1$ μs, I and J are determined from the length of the column ($L = 0.5$ m) and time (12 ms), respectively, $I = 500$, $J = 120000$.

On this grid, all interior nodes with indices $i\in[1, I]$ represent a position inside the cell, where $x_i = i\cdot\Delta x$. The edge nodes, those with indices $i = 0$ and $i = I+1$, represent the upstream and downstream boundaries of the column, while those with indices $j = 0$ represent the initial conditions inside the granular column. Using these points, we make discrete representations for the spatiotemporal evolution of pressure, porosity and particle velocity,

$$\left(P_f\right)_i^j=P_f\left(x_i,t_j\right),\varepsilon_i^j=\varepsilon\left(x_i,t_j\right),\left(u_p\right)_i^j=u_p\left(x_i,t_j\right).$$

Using the first-order forward difference scheme and central difference scheme at the half-point discretizing Eq. (A1) in the time and space directions, we can obtain:

$$\frac{\varepsilon_i^{j+1}\left(P_f\right)_i^{j+1}-\varepsilon_i^j\left(P_f\right)_i^j}{dt}=\frac{1}{\mu}\frac{k_{i+1/2}^j\left(P_f\right)_{i+1/2}^j\frac{\left(P_f\right)_{i+1}^j-\left(P_f\right)_i^j}{dx}-k_{i-1/2}^j\left(P_f\right)_{i-1/2}^j\frac{\left(P_f\right)_i^j-\left(P_f\right)_{i-1}^j}{dx}}{dx}$$
$$+\frac{\varepsilon_{i+1/2}^j\left(P_f\right)_{i+1/2}^j\left[\left(u_p\right)_{i+1/2}^j-u_{comp}\right]-\varepsilon_{i-1/2}^j\left(P_f\right)_{i-1/2}^j\left[\left(u_p\right)_{i-1/2}^j-u_{comp}\right]}{dx} \quad (A2)$$

where the pressure, particle velocity, porosity and permeability at the half point are as follows:

$$\left(P_f\right)_{i-1/2}^j=\frac{\left(P_f\right)_{i-1}^j+\left(P_f\right)_i^j}{2}$$
$$\left(P_f\right)_{i+1/2}^j=\frac{\left(P_f\right)_i^j+\left(P_f\right)_{i+1}^j}{2} \quad (A3)$$

$$\left(u_p\right)_{i-1/2}^j=\frac{\left(u_p\right)_{i-1}^j+\left(u_p\right)_i^j}{2}$$
$$\left(u_p\right)_{i+1/2}^j=\frac{\left(u_p\right)_i^j+\left(u_p\right)_{i+1}^j}{2} \quad (A4)$$

$$\varepsilon_{i-1/2}^j=\frac{2\varepsilon_{i-1}^j\cdot\varepsilon_i^j}{\varepsilon_{i-1}^j+\varepsilon_i^j},\ \varepsilon_{i+1/2}^j=\frac{2\varepsilon_i^j\cdot\varepsilon_{i+1}^j}{\varepsilon_i^j+\varepsilon_{i+1}^j} \quad (A5)$$

$$k_{i-1/2}^j=\frac{2k_{i-1}^j\cdot k_i^j}{k_{i-1}^j+k_i^j},\ k_{i+1/2}^j=\frac{2k_i^j\cdot k_{i+1}^j}{k_i^j+k_{i+1}^j} \quad (A6)$$

By discretizing Eqs. (18) and (19), the spatiotemporal evolution of the porosity and particle velocity of all points with indices $i\in[0, I+1]$ and $j\in[0, J+1]$ are obtained:

$$\varepsilon_i^j=\frac{\varepsilon_0-\varepsilon_{comp}}{2}\cdot\mathrm{erf}\left(4\cdot\frac{x_i-u_{CF}\cdot t_j}{w_{CF}}\right)+\frac{\varepsilon_0+\varepsilon_{comp}}{2} \quad (A7)$$

$$\left(u_p\right)_i^j=-\frac{u_{p,comp}}{2}\cdot\mathrm{erf}\left(4\cdot\frac{x_i-u_{CF}\cdot t_j}{w_{CF}}\right)+\frac{u_{p,comp}}{2} \quad (A8)$$

Using this explicit scheme, all interior points $i\in[1, I]$ at step j can be derived from the information of points $i\in[0, I+1]$ at the previous step j-1:

$$\left(P_f\right)_i^{j+1}=\frac{1}{\varepsilon_i^{j+1}}\left\{\frac{1}{\mu}\frac{dt}{(dx)^2}\left[k_{i+1/2}^j\left(P_f\right)_{i+1/2}^j\left(\left(P_f\right)_{i+1}^j-\left(P_f\right)_i^j\right)\right]-\frac{1}{\mu}\frac{dt}{(dx)^2}\left[k_{i-1/2}^j\left(P_f\right)_{i-1/2}^j\left(\left(P_f\right)_i^j-\left(P_f\right)_{i-1}^j\right)\right]\right.$$
$$+\frac{dt}{dx}\left\{\varepsilon_{i+1/2}^j\left(P_f\right)_{i+1/2}^j\left[\left(u_p\right)_{i+1/2}^j-u_{comp}\right]\right\}$$
$$\left.-\frac{dt}{dx}\left\{\varepsilon_{i-1/2}^j\left(P_f\right)_{i-1/2}^j\left[\left(u_p\right)_{i-1/2}^j-u_{comp}\right]\right\}+\varepsilon_i^j\left(P_f\right)_i^j\right\} \quad (A9)$$

Considering the boundary conditions for Eq. (A9), the pressure at the upstream surface approximately equals the pressure when an incident shock wave is reflected head-on from a solid boundary, P_r, as shown in Eq. (16). Before the completion of the filtration process, the pressure at the downstream surface is kept ambient pressure P_0 unchanged:

$$P_f\left(0, t_{0,1,\cdots,J,J+1}\right)=P_r \quad (A10)$$

$$P_f\left(L, t_{0,1,\cdots,J,J+1}\right)=P_0 \quad (A11)$$

At the starting moment of the flow filtration process, the pressure inside the column is ambient pressure P_0. Thus, the initial conditions for the interior points are:

$$P_f\left(x_{1,2,\cdots,I-1,I}, 0\right)=P_0 \quad (A12)$$

With solutions from Eq. (A9), together with the given boundary conditions and initial conditions in Eqs. (A10)–(A12), the evolution of the unsteady filtration pressure field over time is obtained.

References

Apte, S., Mahesh, K., Lundgren, T., 2003. A Eulerlan-Lagrangian Model to Simulate Two-Phase/Particulate Flows. Center for Turbulence Research Annual Research Briefs, pp. 161–171.

Baer, M.R., Nunziato, J.W., 1986. A two-phase mixture theory for the deflagration-to-detonation transition (ddt) in reactive granular materials. Int. J. Multiphas. Flow 12 (6), 861–889. https://doi.org/10.1016/0301-9322(86)90033-9.

Borchardt-Ott, W., 2012. Crystallography: An Introduction. https://doi.org/10.1007/978-3-642-16452-1.

Britan, A., Ben-Dor, G., 2006. Shock tube study of the dynamical behavior of granular materials. Int. J. Multiphas. Flow 32 (5), 623–642. https://doi.org/10.1016/j.ijmultiphaseflow.2006.01.007.

Britan, A., Ben-Dor, G., Igra, O., Shapiro, H., 2006. Development of a general approach for predicting the pressure fields of unsteady gas flows through granular media. J. Appl. Phys. 99 (9), 093519. https://doi.org/10.1063/1.2197028.

Britan, A., Ben-Dor, G., Igra, O., Shapiro, H., 2001. Shock waves attenuation by granular filters. Int. J. Multiphas. Flow 27, 617–634. https://doi.org/10.1016/S0301-9322(00)00048-3.

Britan, A., Shapiro, H., Ben-Dor, G., 2007. The contribution of shock tubes to simplified analysis of gas filtration through granular media. J. Fluid Mech. 586,

147–176. https://doi.org/10.1017/s0022112007006878.
Carmouze, Q., Saurel, R., Chiapolino, A., Lapebie, E., 2020. Riemann solver with internal reconstruction (RSIR) for compressible single-phase and non-equilibrium two-phase flows. J. Comput. Phys. 408, 109176. https://doi.org/10.1016/j.jcp.2019.109176.
Chiapolino, A., Saurel, R., 2020. Numerical investigations of two-phase finger-like instabilities. Comput. Fluid 206, 104585. https://doi.org/10.1016/j.compfluid.2020.104585.
Crowe, C.T., Schwarzkopf, J.D., Sommerfeld, M., Tsuji, Y., 2012. Multiphase Flows with Droplets and Particles. CRC Press, Boca Raton.
Di Felice, R., 1994. The voidage function for fluid-particle interaction systems. Int. J. Multiphas. Flow 20, 153–159. https://doi.org/10.1016/0301-9322(94)90011-6.
Ergun, S., 1952. Fluid flow through packed columns. J. Chem. Eng. Prog. 48, 89–94.
Eriksen, F.K., Toussaint, R., Turquet, A.L., Mly, K.J., Flekky, E.G., 2018. Pressure evolution and deformation of confined granular media during pneumatic fracturing. Phys. Rev. E. 97 (1), 012908. https://doi.org/10.1103/PhysRevE.97.012908.
Goodarzi, M., Mohammadi, S., Jafari, A., 2015. Numerical analysis of rock fracturing by gas pressure using the extended finite element method. Petrol. Sci. 12, 304–315. CNKI:SUN:SYKX.0.2015-02-009.
Jafari, A., Hasani, M., Hosseini, M., Gharibshahi, R., 2020. Application of CFD technique to simulate enhanced oil recovery processes: current status and future opportunities. Petrol. Sci. 17, 434–456. https://doi.org/10.1007/s12182-019-00363-7.
Jagadeesh, G., 2008. Fascinating world of shock waves. Resonance 13 (8), 752–767. https://doi.org/10.1007/s12045-008-0082-1.
Koneru, R.B., Rollin, B., Durant, B., Ouellet, F., Balachandar, S., 2020. A numerical study of particle jetting in a dense particle bed driven by an air-blast. Phys. Fluids 32 (9), 093301. https://doi.org/10.1063/5.0015190.
Kruggel-Emden, H., Sturm, M., Wirtz, S., Scherer, V., 2008. Selection of an appropriate time integration scheme for the discrete element method (DEM). Comput. Chem. Eng. 32 (10), 2263–2279. https://doi.org/10.1016/j.compchemeng.2007.11.002.
Levy, A., Ben-Dor, G., Skews, B.W., Sorek, S., 1993. Head-on collision of normal shock waves with rigid porous materials. Exp. Fluid. https://doi.org/10.1007/BF00189885.
Li, J., Xue, K., Zeng, J., Tian, B., Guo, X., 2021. Shock-induced interfacial instabilities of granular media. J. Fluid Mech. 930. https://doi.org/10.1017/jfm.2021.912.
Liu, X., S. O., T. C, 1994. Weighted essentially non-oscillatory schemes. J. Comput. Phys. 115 (1), 200–212. https://doi.org/10.1006/jcph.1994.1187.
Meng, B., Zeng, J., Tian, B., Li, L., He, Z., Guo, X., 2019. Modeling and verification of the Richtmyer–Meshkov instability linear growth rate of the dense gas-particle flow. Phys. Fluids 31 (7), 074102. https://doi.org/10.1063/1.5099996.
Michiru, Y., Seiji, W., Kazutaka, K., Tetsuya, Y., Mitsuru, M., 1996. Experiment on effects of porosity in the Interaction of shock wave and foam. JSME Int. J. Ser. B Fluids Therm. Eng.
Morrison, F.A., 1972. Transient gas flow in a porous column. Ind. Eng. Chem. Fundam. 11 (2), 191–197. https://doi.org/10.1021/i160042a008.
Osnes, A.N., Vartdal, M., Pettersson Reif, B.A., 2017. Numerical simulation of particle jet formation induced by shock wave acceleration in a Hele-Shaw cell. Shock Waves. https://doi.org/10.1007/s00193-017-0778-9.
Poroshyna, Y.E., Utkin, P.S., 2021. Numerical simulation of a normally incident shock wave – dense particles layer interaction using the Godunov solver for the Baer–Nunziato equations. Int. J. Multiphas. Flow 142, 103718. https://doi.org/10.1016/j.ijmultiphaseflow.2021.103718.
Skews, B.W., 2001. Handbook of Shock Waves || Shock Wave Propagation in Multiphase Media, pp. 545–596. https://doi.org/10.1016/B978-012086430-0/50032-4.
Sundaresan, S., Ozel, A., Kolehmainen, J., 2018. Toward constitutive models for momentum, species, and energy transport in gas–particle flows. Annu. Rev. Chem. Biomol. Eng. 9 (1), 61–81. https://doi.org/10.1146/annurev-chembioeng-060817-084025.
Thallak, S., 1991. Numerical Simulation of Hydraulic Fracturing in Granular Media. University of Waterloo (Canada). [Ph. D. dissertation].
Tian, B., Zeng, J., Meng, B., Chen, Q., Guo, X., Xue, K., 2020. Compressible multiphase particle-in-cell method (CMP-PIC) for full pattern flows of gas-particle system. J. Comput. Phys. 418, 109602. https://doi.org/10.1016/j.jcp.2020.109602.
Toro, E.F., 2009. Riemann Solvers and Numerical Methods for Fluid Dynamics || the HLL and HLLC Riemann Solvers, pp. 315–344. https://doi.org/10.1007/b79761.
Ukai, S., Balakrishnan, K., Menon, S., 2010. On Richtmyer–Meshkov instability in dilute gas-particle mixtures. Phys. Fluids 22 (10), 104103. https://doi.org/10.1063/1.3507318.
van der Grinten, J.G.M., van Dongen, M.E.H., van der Kogel, H., 1985. A shock-tube technique for studying pore-pressure propagation in a dry and water-saturated porous medium. J. Appl. Phys. 58 (8), 2937–2942. https://doi.org/10.1063/1.335841.
Waitukaitis, S.R., Roth, L.K., Vitelli, V., Jaeger, H.M., 2013. Dynamic jamming fronts. EPL 102 (4), 44001. https://doi.org/10.1209/0295-5075/102/44001.
Xie, Y., Feng, F., Li, Y., Hu, Z., Shao, J., Mei, Y., 2021. Molecular dynamics simulation of shock-induced structural change and permanent densification of silica glass: the effect of initial density. Mech. Mater. 159, 103913. https://doi.org/10.1016/j.mechmat.2021.103913.
Xu, Z., Li, S., Li, B., Chen, D., Liu, Z., Li, Z., 2020. A review of development methods and EOR technologies for carbonate reservoirs. Petrol. Sci. 17 (4), 990–1013. https://doi.org/10.1007/s12182-020-00467-5.
Xue, K., Shi, X., Zeng, J., Tian, B., Han, P., Li, J., Liu, L., Meng, B., Guo, X., Bai, C., 2020. Explosion-driven interfacial instabilities of granular media. Phys. Fluids 32 (8), 084104. https://doi.org/10.1063/5.0014039.
Yan, G., Yu, H.S., Mcdowell, G., 2009. Simulation of granular material behaviour using DEM. Procedia Earth Planetary Sci. 1 (1), 598–605.
Zhang, L., Feng, Z., Sun, M., Guan, H., Jin, H., Shi, H., 2022. Modeling of long-term shock interaction with a movable particle curtain in a rectangular tube based on a dense discrete phase model. Powder Technol. 415, 118116. https://doi.org/10.1016/j.powtec.2022.118116.

Glossary

English letters

C_d: dimensionless drag force coefficient
d: diameter, m
D_p: drag force coefficient, s^{-1}
e: specific internal energy, J/kg
E: total energy, J
F: force, N
F_C: the collision force, N
F_{drag}: the drag force, N
F_{PP}: the pressure gradient force, N
k: permeability, m^2
k_p: stiffness, N/m
L: length of granular column, m
m: mass, kg
M_s: mach number
P: pressure, N/m^2
P_r: reflected pressure of the incident shock, N/m^2
$P_{upstream}$: the pressure at the moving upstream surface, N/m^2
r: particle radius, m
Re_p: particle Reynold number
sg: specific gravity
t: time, s
$\tilde{t}$: the scaled time
t_{ini}: the short period of time for the pressure at the moving upstream surface to increase, s
t_{sc}: the scaling factor for the time, s
t_{st}: the scaled time required for the compaction front to reach steady state
T: temperature, K
$\tilde{T}$: the scaled temperature
T_r: temperature at the upstream surface of the granular column, K
u: velocity, m/s
$\tilde{u}$: the scaled velocity
$u_{p,comp}$: velocity of shock compacted particles, m/s
$\tilde{u}_{p,comp}$: the scaled $u_{p,comp}$
V_{CF}: the propagation velocity of the compaction front, m/s
$\tilde{V}_{CF}$: the scaled V_{CF}
V_{sc}: the scaling factor for the velocity, m/s
$\tilde{w}$: the scaled width of the compaction front
w_{CF}: the width of the compaction front, m
$\tilde{x}$: the scaled distance by particle diameter
x_{CF}: the distance of the compaction front from the upstream surface of the granular column, m

Greek letters

α^2: super particle loading
χ: the scaled distance by length of the particle column
$\Delta\tilde{u}_{spike}$: amplitude of the scaled gas velocity spike
$\Delta\tilde{T}_{spike}$: amplitude of the scaled temperature spike
δ: overlap, m
ε: porosity
ε_p: restitution coefficient of the parcel
φ: volume fraction
φ_0: the initial volume fraction of the particle column
$\varphi_{0,cr}$: the critical initial volume fraction of the particle column to form velocity and temperature spikes
φ_{local}: local volume fraction of particles calculated through Voronoi tessellation
φ_{comp}: volume fraction of compacted particles
γ: ratio of specific heat
γ_p: damping coefficient of parcel
μ: dynamic viscosity, $N\cdot s/m^2$
θ: the scaled pressure
$\theta_{deflect}$: the scaled deflection pressure
$\theta_{plateau}$: the scaled steady deflection pressure
ρ: density, kg/m^3
$\tilde{\rho}$: the scaled density

Subscripts

f: fluid phase
n: normal direction
p: computational particle